Summer 2018

Designed extrudate for ceramic additive manufacturing

Devin McMillen

Follow this and additional works at: https://scholarsmine.mst.edu/masters_theses

Part of the Materials Science and Engineering Commons, and the Mechanical Engineering Commons
Department:

Recommended Citation

DESIGNED EXTRUDATE FOR CERAMIC ADDITIVE MANUFACTURING

by

DEVIN THOMAS MCMILLEN

A THESIS

Presented to the Faculty of the Graduate School of the

MISSOURI UNIVERSITY OF SCIENCE AND TECHNOLOGY

In Partial Fulfillment of the Requirements for the Degree

MASTER OF SCIENCE IN MANUFACTURING ENGINEERING

2018

Approved by

Ming C. Leu, Advisor

Greg E. Hilmas

Jeremy L. Watts

ABSTRACT

The objective of this thesis work was to design ceramic paste systems that assist in achieving a high theoretical density (>95%) after deposition by a novel additive manufacturing process, i.e. Ceramic On-Demand Extrusion (CODE). The work is encompassed in five main sections: Sections 1 and 2 provide an introduction and literature review of relevant topics for the following sections of experimentation. Section 3 provides an analysis of a reaction chemistry to identify three discrete materials that could be combined via CODE and result in zirconium diboride (ZrB_2) post-sintering. Section 4 describes the development of a high solids loading, aqueous yttria-stabilized zirconia paste. This material was identified as the next viable technical ceramic system after alumina for addition to the CODE portfolio. Section 5 details the use of sol-synthesized pre-mullite composite powder to densify stoichiometric mullite at modest temperatures. Section 6 provides a conclusion to the research results provided in the preceding three sections, as well as future work outlined in Section 7.

ACKNOWLEDGMENTS

I would like to first thank my advisor, Dr. Ming Leu, for this unique opportunity and believing in my abilities as a ceramic engineer. I would also like to thank Dr. Greg Hilmas for being a constant source of technical advice and guidance, as well as Dr. Jeremy Watts for acting as a mentor in the lab and always having an open door. I have learned a great deal from my committee in two years and will forever be grateful for the guidance I received. Also, I would be remiss if I did not thank Wenbin Li and Amir Ghazanfari who welcomed me into this project and put up with me disrupting the status quo. I could not forget Dr. Mary Reidmeyer, who continues to be someone I look up to as a model– a true engineer and indispensable resource.

I would also like to thank the entire UHTC graduate group: Paul Brune, Austin Stanfield, Alec Murchie, Ryan Grohsmeyer, Eric Neuman and others for constantly being there to exchange ideas, and the AMCL staff for their indelible support and guidance.

TABLE OF CONTENTS

LIST OF ILLUSTRATIONS

LIST OF TABLES

1. INTRODUCTION

The objective of this thesis work was to design ceramic paste systems for room temperature deposition via Ceramic On-Demand Extrusion for fabricating parts with overhangs, voids, embedded components, or complex patterning, and achieve a high relative bulk density after post processing. The design criteria included: solids loading, solvent pH, dispersion strategy, dispersant type, sintering time, and sintering temperature. This was applied to three separate ceramic systems to develop: 1) a proof-of-concept chemistry for *in situ* fabrication of zirconium diboride that would be compatible with stereolithography technology; 2) a yttria stabilized zirconia paste for deposition of complex parts; and 3) a mullite system that would be compatible with alumina for use in a graded composite.

For the fabrication of high-temperature sensors with components embedded into a ceramic matrix, the additive manufacturing method named Ceramic On-Demand Extrusion (CODE) was developed [1]. This technique, similar to Direct-Write Assembly [2], Direct Ink Writing [3], or Robocasting [4], is a novel and robust method for additive manufacturing (AM) of technical ceramics using extrusion-based AM techniques; already a small field of research, few other techniques are capable of successfully fabricating fully dense ceramic parts, e.g. stereolithography and powder bed fusion [5]. Using high solids loading (>50 vol%), aqueous, ceramic extrudate, deposition is done at room temperature to build a 3D geometry layer-upon-layer. After deposition, each layer is partially solidified by uniform infrared radiation applied perpendicular to the top face. Concurrently, the built portion is surrounded, flush with the top most layer, by a low molecular weight oil to promote one-dimensional drying. Drying in this way eliminates a water content gradient in the deposited part, imparting greater structural stability during the build, and enables the production of ceramic parts free of fracture and warpage.

With proper control of deposition and drying, the design of extrudate is essential to prevent the introduction of flaws. An inhomogeneous paste not only affects the bulk article, but also its deposition. Inconsistent deposition and density gradients will lead to a low density bulk, if not outright failure during sintering. For materials like stoichiometric

mullite, multi-hour isothermal holds are necessary for the densification of the bulk and phase development. These steps are detrimental to processing efficiency, making it more desirable to use a system that reaction sinters, utilizes transient sintering, or has a submicron initial particle size.

Sintering of non-oxide ceramics is often difficult because of their high melting temperature, due to strong covalent bonds (metallic, ionic, and covalent in the case of zirconium diboride) [6]. Sintering to high densities is normally achieved through solid-state sintering by pressure-assisted methods, such as hot pressing and hot isostatic pressing. However, these methods limit production to the creation of monolithic geometries, and as such, are not viable for complex geometries often associated with additive manufacturing. Alternative pressureless processing routes have proven equally successful [7], [8]. Pressureless sintering is the promotion of densification without the application of an external pressure upon a body. This is the most common sintering method and often what is referred to when 'sintering' a ceramic body [9]. Zirconium diboride (ZrB_2) is classified as an ultrahigh temperature ceramic (UHTC), which have melting temperatures over $3000^{\circ}C$ [10]. This class of material performs well in harsh environments, often exceeding the capabilities of traditional engineering materials.

Reaction sintering is a method in which both chemical reaction and densification occur in a single sintering cycle. Normally a method reserved for production of high purity powders, several reaction paths have been introduced with varying thermodynamic requirements [11], [12]. However, none have been applied to *in situ* fabrication using additive manufacturing (AM). With application of colloidal processing techniques, an extrudate may be designed, such that it has the desired rheological properties for deposition, the chemistry for reaction sintering, and a particle size to promote specific phase development [13]. These parameters can be further controlled to promote high relative density without pressure-assisted sintering, such that complex, near net-shape components may be fabricated. Elimination of the machining costs associated with ceramic materials would alone justify *in situ* fabrication. The structural and thermal properties of ZrB_2 are valuable to many industries that would favor a method of

production that provides a high degree of compositional control with low machining costs.

Pressureless reaction sintering, applied to CODE, provides a solution to *in situ* fabrication of near net-shape UHTC components with a high degree of microstructural control and minimal post-processing that has not yet been achieved in AM to date. This thesis work uses the following three sections to describe (Section 1.) the initial investigation to design an oxide-carbide-nitride extrudate to fabricate highly complex near net-shape components, (Section 2.) development of a high solids loading yttrium oxide-stabilized zirconium oxide (3YSZ) paste, and (Section 3.) identification of a method for synthesizing mullite at low temperatures and times.

2. LITERATURE REVIEW

2.1. STATE OF CERAMIC ADDITIVE MANUFACTURING

In 2010, the American Society for Testing and Materials (ASTM) established the committee ASTM F42 – *Additive Manufacturing*, to set standards for additive manufacturing (AM) processes and technology. This committee differentiated the types of AM processes into seven categories: binder jetting, directed energy deposition, material extrusion, material jetting, powder bed fusion, sheet lamination, and vat photopolymerization [14]. However, ASTM F2792 was withdrawn in 2015 with no replacement after a tri-annual review of the terms, nomenclature, and acronyms defined within. It was replaced with a more generalized document by ASTM subcommittee F42.01 *on Terminology* that same year, titled ISO/ASTM 52900:2015 *Standard Terminology for Additive Manufacturing- General Principles – Terminology*. Like its predecessor, ASTM 52900 seeks to define new terms and processes accurately and consolidate terminology used by AM users in industry, academic, and media. ISO/ASTM 52900 is due for evaluation this year for revision and update.

A review published by Guo and Leu (2013), noted that polymers are the main focus of AM research, with the major processing having starting materials of liquid resins, extrudates, powder bed, or solid sheets[15]. They also acknowledged that metal AM has been studied enough in the literature to have established processing methods that yield dense components with mechanical properties comparable to the bulk metal. Furthermore, they noticed that there is significant potential in fields from aerospace to energy, but the technology is considered a niche in industry. Another review that year, published by Vaezi et al. (2013), focused on multiple material additive manufacturing (MMAM), which was described as a process that does not have pre-mixed or composited raw materials, or secondary integration by infiltration, coating, or a non-AM post process. Vaezi et al. considered all seven groups outlined by ASTM but concluded that material jetting and material extrusion processes were most compatible with MMAM. In terms of ceramic additive manufacturing, the most recent reference considered was 2011, and it was predicted that inkjet printing would be the best method for fabrication of components

such as capacitors and sensors, as well as conductive thick films, with extrusion deposition leading the way for bioceramics [16].

A second review by Vaezi et al. (2013), focused on the state of micro-additive manufacturing technologies, and featured technical ceramics systems more so than the previous MMAM review. Of the key micro-AM systems, micro-stereolithography (MSL), microlaser sintering (MLS), three-dimensional printing (3DP), inkjet printing, and laminated object manufacturing (LOM) were amenable to ceramic fabrication. MSL, 3DP, LOM, and, like the previous review, extrusion-based processes, were capable of producing relatively dense parts (< 20 % porosity) [17]. Lithography AM techniques, such as digital light processing (DLP), have been used to fabricate dense zirconia parts using resins with 45 vol% solid loading. Mitteramskolger et al. (2014) demonstrated that by controlling the depth of cure parameter and designing for light scattering distortion of their DLP system, sub-pixel resolution can be obtained, i.e. 25 µm, as well as no fracture after debinding for their zirconia samples [18]. However, Mitteramskolger et al. did not provide the percent theoretical density of their sintered specimens. Though lithography has the highest resolution of AM techniques (in the range of 20-100 µm), the vol% of resin is detrimental to densification [19], [20].

The most thorough review of additive manufacturing of ceramics was Travitzky et al. (2014); the publication focused solely on ceramic materials [21]. In the publication, a table summarized what ceramic materials could be fabricated by 3DP, selective laser sintering (SLS), stereolithography (SLA), extrusion freeform fabrication (EFF), and LOM, characterized as structural, functional, or bioceramics. Of the techniques discussed, LOM and EFF can directly produce dense ceramics. LOM is amenable to fabricating dense non-oxide ceramics, such as silicon nitride (Si_3N_4), because the process uses a preceramic paper or cast tape. Such parts have been fabricated by Rodrigues et al. (2000) with a relative density of 97% when sintered at 1750°C for 2 hr [22]. The resultant mechanical properties were dependent on whether or not the greenforms were infiltrated with a polyurea-silazane resin: un-infiltrated LOM parts had a Young's modulus of 307 GPa, an average room temperature flexural strength of 918 MPa, and a fracture toughness of 7.45 MPa·$\sqrt{m}$, which they found comparable to traditionally fabricated Si_3N_4.

Infiltrated parts exhibited lower mechanical properties due to increased flaw population from the infiltration process, with a Young's modulus of 301 GPa, flexural strength of 707 MPa, and fracture toughness of 5.42 MPa·$\sqrt{m}$. Even the density of the infiltrated part was lower at 3.142 g/cm^3, versus the uninfiltrated parts at 3.248 g/cm^3.

SLA has continued to be the technique of choice for those fabricating non-oxide ceramics, especially silicon oxycarbide (SiOC). The HRL Laboratories demonstrated a SiOC microlattice using SLA and pyrolysis of the preceramic polymer to synthesize SiOC [23]. They identified a mixture of UV-curable siloxane resins compatible with a photoinitiator and fabricated several complex microlattice geometries. Concurrently, de Hazan (2016), also using SLA, modified a polycarbosilane system with nonpolar acrylate monomers to make SiC and SiOC mesoscale lattices, though with pore volumes ranging from 0.024-.33 cm^3/g in the solid specimens [24].

The most historically notable EFF technique to be discussed was robocasting (RC). Using this technique, less than 1% organics can be used to fabricate and dry a part within 24 hr, with an aqueous extrudate deposited on a heated plate to induce dilatancy by drying the deposited shape. The historical portfolio of material systems included alumina, alumina:Al composites, alumina:Mo composites, lead zirconate titanate, zinc oxide, kaolin, stabilized zirconia, and mullite [25]. Due to its use of high solids loading extrudate, RC has been continued to be used for piezoelectric monolithic and composite geometries [25], mesoscopic spanning structures [27], as well as near-net-shaped components of a variety of designed extrudates [28].

Freeze-form Extrusion Fabrication (FEF) was developed in response to size limitations of other EFF techniques, such as development of drying gradients, and resulting fracture, during robocasting of mesoscale architectures. FEF was intended to be environmentally friendly, i.e. the systems were predominantly aqueous, and deposited in a temperature-controlled chamber, onto a sub-0°C substrate to solidify high solids loading pastes. This allowed for the fabrication of thick-walled specimens with paste systems of varying densities (3.986 – 15.63 g/cm^3). The extrusion mechanism was extensively modeled and optimized for ram force-controlled deposition, as well as the effect of environment temperature on build quality [29], [30], [31]. With the optimization of early

FEF designs, systems were developed to deposit alumina [32], [33], 13-93 bioactive glass [34], [35], and three-component systems for functionally graded composites [36].

Extrusion freeform fabrication techniques have a broader portfolio in the literature concerning technical ceramics, structural ceramics, as well as biomaterials. Extrusion principles are widely known, due to industry use, so customizable printers are easily designed and built. W. Li et al. demonstrated this by developing the CODE system to improve upon FEF and applied colloidal processing techniques, i.e. particle size control and pH control, to fabricate stabilized zirconia parts [37]. Other research groups have recognized the ease of use and popularity and have built similar systems for their research needs [38]. Bioprinting is a general term used to describe the extrusion deposition of organic carrier systems loaded with bioactive materials. This EFF technique has been applied to biomaterial systems like PCL/borate glass composites [39] and calcium silicate/calcium phosphate scaffolds [40].

2.2. COLLOIDAL PROCESSING OF CERAMICS

Control of interparticle forces is key for stability of dispersed powders in a liquid suspension. A colloidal dispersion is a system in which a particulate is homogeneously dispersed in a continuous phase, e.g. distilled water. One dimension of the dispersed phase (colloid) must be within the submicron range ($< 10^{-6} – 10^{-9}$ m) and are often nanoparticles or macromolecules. The interface of the colloid and the continuous phase controls the surface properties of the colloid: surface charge, electric double layer, and adsorption. These properties are key to homogeneous dispersion and stability, which is the summation of particle interaction, particle-solution interaction, and solution-solution interaction; the continuous phase could more generally be called a medium, if not an aqueous solution [41].

When a ceramic particle, i.e. an oxide, is put into water and the surface is hydrated the surface chemistry is represented by either equation (1) or (2) depending on the material's isoelectric point (IEP):

$$MOH_{2\ (surface)}^{+} \leftrightarrow MOH_{(surface)} + H_{(surface)}^{+} \qquad (1)$$

$$MOH_{(surface)} \leftrightarrow MO^-_{(surface)} + H^+_{(solution)} \tag{2}$$
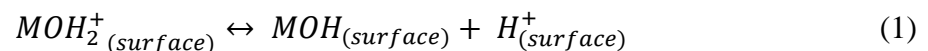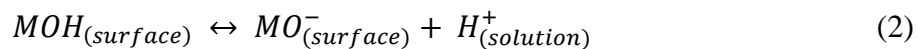
where M represents a metal ion on the surface, such as Al^{3+} and is bonded to a bulk oxygen ion to satisfy electronegativity. The point of zero charge (PZC) is the average of the rate values of the reaction, which describes the acid-base character of the surface. Hydrated surfaces of an oxide in pure water will have reactions determined only by H_3O^+ and OH^-. The pH value when the protonation and deprotonation is in equilibrium, the PZC, is termed the isoelectric point. Exchange at the surface of the oxide is reversible, time dependent, and potential determining, meaning dissolution of a particle is minimized at the PZC. If there are ions in solution, they may neutralize surface sites, or build up into a diffuse double layer of ions and counter ions. When two particle double-layers interact, the potential this causes or the energy barrier due to competing attractive and repulsive forces in solution is called DLVO Theory (named after Derjaguin, Landau, Verwey, and Overbeek) [42].

Generally, there are three methods to stabilize a dispersion, which are described by the interaction potential at a specific scale: 1) electrostatically ($2\kappa^{-1}$), 2) sterically (2δ), and 3) structural contributions (σ), shown in Figure 2.1. Electrostatic stabilization occurs when enough charges of the same kind and magnitude are generated on a surface, shown in Figure 2.1A. The resulting electrostatic potential is exponentially dependent upon the distance from the surface, and the strength depends on the potential induced on an interacting surface as well as the dielectric property of the medium. This is predicted by DLVO theory, where dispersions are destabilized by shifting the pH toward the IEP or increasing the solution ionic strength. The network of ions and counterions that make up the diffuse double layer are then described by κ^{-1}.

Steric stabilization occurs due to strong adsorption of an organic molecule, with enough surface site density to overcome van der Waals attraction, shown in Figure 2.1B. The conformation of the adsorbed layer is highly dependent upon solvent quality, the adsorbed molecular structure, adsorption density, and concentration in solution. This adsorbed layer is called the adlayer, δ. The adsorbed species may be a polyelectrolyte, which provides steric and electrostatic stabilization, a subtype called electrosteric

stabilization. A polyelectrolyte will have at least one ionizable group, e.g. carboxylic, and may be homopolymers or co-block polymers with multiple ionizable segments. Electrosteric stabilization is highly susceptible to surface and solvent chemistry, so adsorption is favorable when the ionized group and surface have opposite charges. At low concentrations, a species can promote flocculation due to surface charge neutralization or bridging between surfaces. The conformation is also susceptible to solvent conditions, i.e. pH and ionic strength. Low pH will cause organic chains to coil up densely, creating a low adlayer thickness, while a high pH causes full ionization and an open configuration occurs due to intersegment repulsion [43], [44].

Structural contributions to stabilization, called depletion stabilization, refers to the depletion forces that occur between the "large" colloidal particles in solution with smaller, nonadsorbed species between, e.g. polymers/oligomers/monomers or finer colloids, shown in Figure 2.1C. These species, called depletants, may promote flocculation or stabilization of the primary colloidal species, where depletion refers to the existence of a negative concentration gradient near the primary surface. Stable dispersions may undergo a transition from stable, to depletion flocculation, to depletion stabilization as the depletant volume fraction increases. Destabilization occurs when the depletant is excluded from the interparticle gap and flocculation potentially occurs due to an osmotic pressure differential. The scale for depletion forces, σ, are related to the depletant diameter, and in some cases the medium (solvent) diameter [45].

For dispersions with a solids loading $\varphi > 0.4$, there is a structure that develops between the surfaces, which can be described as a particulate gel, in the case of ceramic dispersions. This is due to the potential between the particles or the steric interaction of adsorbed species. Due to the close proximity of interacting surfaces, ΔpH or Δ[ionic strength] will have a significant and disparate impact on the gel structure. Any change in the pH alone may be used to identify the system pH_{IEP}, which is now highly sensitive due to $\varphi > 0.4$. A similar change will be seen with Δ[ionic strength], a response which describes the colloid's electrophoretic mobility, or the zeta potential, ζ.
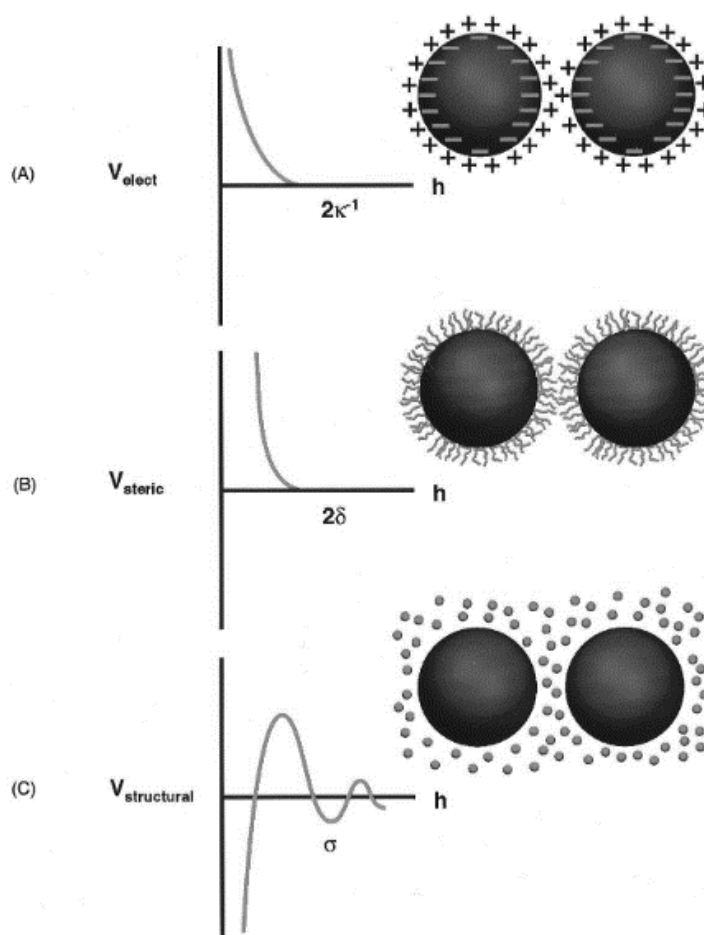
Figure 2.1. Representation of interaction potentials between two particles in suspension and their respective scale length for (A) electrostatic, (B) steric, and (C) depletion forces.

That is to say that near the IEP or at the lowest zeta potential value, the dispersion is destabilized and will sediment, while the highest zeta potential value for a range of pH and ionic strength identifies stability [46]. The state of the gel structure can be measured with static light scattering, dynamic light scattering (DLS), diffuse wave spectroscopy, small-angle x-ray scattering (SAXS), small angle neutron scattering (SANS), dynamic rheology with confocal microscopy, or more simply with a dispersion study. How the dispersion is designed, the particle size, solids loading, solvent, pH, ionic strength, and

temperature, will all affect the final characteristic of the dispersion rheology, mechanical and optical properties [47].

2.3. SINTERING OF CERAMICS

The process step involving the heat treatment of the debinded green body for conversion into a functional solid is referred to as firing or sintering. There are four categories of sintering: solid-state, liquid-phase, viscous, and vitrification. There are also sintering under an externally applied load and reaction sintering. For the following studies, only solid state, viscous, and reaction sintering will be discussed. The categories of sintering describe both the driving force for sintering as well as how matter is transported. Sintering is an irreversible process and driven by the reduction of free energy in the system, which for the case of solid-state sintering is the reduction of surface area of a green body. There are three stages to sintering. During the initial stage, atomic mobility begins, concave necks form between particles, and typically 3-5% linear shrinkage occurs. This stage ends around 65% relative density. The second stage is characterized by elimination of high curvature contacts between particles and the bulk becomes a network of solid grains with continuous pores at the edges of grains. This stage ends with approximately 90% relative density. The final stage is the reduction of pore radius and isolation at grain triple-junction corners. Pores are assumed to shrink and disappear altogether in the idealized model, with monosized spheres [48].

Particle size and shape is a major factor in sintering, affecting surface as well as coordination number, which is based on a spherical, monosized model. In a powder compact, if the particle size is such that the coordination number, N, is less than 6, the intergranular porosity will shrink. If the coordination number is equal to six, theoretically the pore growth is metastable, but if the coordination number is high ($N > 6$) the pore may grow. In solid-state sintering, the coordination number of the particles in a compact greatly affects the resultant porosity after sintering. However, sintering occurs via diffusion of material. There are six mechanisms, but only half contribute to densification: grain boundary diffusion, lattice diffusion from the grain boundary to the pore, and plastic flow by dislocation motion [49], [50].

Viscous sintering is a conditional form of liquid-phase sintering. It is limited by the viscosity of the liquid that forms and can generally be thought of in terms of liquid-phase sintering. So, liquid-phase or viscous sintering involves the formation of a liquid that wets and separates the solid phase, facilitating easier rearrangement and material diffusion. For strict viscous sintering states, material diffusion is higher than solid-state, but lower than pure liquid-state sintering. Like solid-state sintering, liquid-phase sintering is described in three stages. The first stage is formation of the liquid, rearrangement of the solid phase, and distribution of the liquid by capillary forces. The second stage is slower as the liquid phase penetrates the solid at the grain boundaries, dissolves the solid, and diffuses the dissolved material through the liquid to areas with lower chemical potential. This redistributed solution is reprecipitated in the regions of lower chemical potential to cause grain coarsening. The final stage is dominated by densification of the solid, coarsened grain network via grain shape accommodation. This means that liquid is distributed away from more efficiently packed regions of grains into open porosity, or from the compact if not reprecipitated [51].

Reaction or reactive sintering specifies a process in which new phases form during sintering. During solid-state and liquid-phase sintering, some reaction occurs between the start and end of the heat treatment that is resolved during the final isothermal soak; this is considered transient reaction sintering because the secondary phase that forms is absorbed. Reaction sintering is defined as a synthesis process by which the major phase is resultant from the two or more reactant components. The reactants may be solid:solid, solid:liquid, or solid:gas, and involve free energy reduction through chemical reaction that is larger than the change in free energy from surface area reduction [52]. This could be done via the ammonolysis of porous silica to yield oxynitride powders [53], magnetron sputtering for nanoparticles of designed core/shell arrangement [54], high purity mullite from β-cristobalite and diaspore ($HalO_2$) [55], or a powder mixture of ZrH_2, Al, and C to synthesize the MAX phase Zr_2AlC [56]. The possibilities for reaction sintering are vast, but limitations arise when reactions are incomplete, unexpected phases form, or are not thermodynamically favorable, which can complicate or hinder densification processes [57].

2.4. RELEVANT SYSTEMS AND THEIR ENGINEERING DESIGN CRITERIA

2.4.1 Zirconium Diboride. ZrB_2 has a high melting temperature (3245°C), high Young's modulus (526 GPa), high hardness (23 GPa), and a theoretical density of 6.09 g/cm^3 [58], [59]. The application of additive manufacturing for UHTCs may provide a cost-effective method for fabrication of complex components for next-generation gas turbines, rocket engines, and hypersonic vehicles [60]. Multiple sintering additives have been found to assist in pressureless sintering of ZrB_2: 1.7 wt% carbon sintered at 1900°C and 4.5 wt% B_4C sintered at 1850°C resulted in near theoretical density for powder attrition milled with tungsten carbide (WC) media [61].

2.4.2 Stoichiometric Mullite. Mullite has several promising engineering properties which include heat resistance, high strength (200-500 MPa), thermal (~1500°C) and chemical stability, low thermal expansion coefficient (4 X 10^{-6}/^{o}C in 20° to 200°C), and high creep resistance [62]. Due to its thermal stability and creep resistance, mullite is an excellent option as a ceramic coating material. It has also been used as fiber reinforcement for thermal and electrical insulation. Traditional consolidation routes require hot-pressing above 1500°C or pressureless sintering above 1650°C; low temperature processing (900-1500°C) for the formation of single-phase mullite can be achieved using chemically synthesized powders and colloidal methods [63].

The synthesis of a composite powder via a sol-gel technique described by Schneider et al. yields a powder with an Al_2O_3 core and a coating of amorphous silica [64]. Upon heat treatment and sintering, the proximity of the precursor material as well as the initial particle size drastically reduces the required sintering temperature (900-1200°C), time for formation, and densification [65]; these steps are shown in Figure 2.2. This procedure uses tetraethyl orthosilicate (TEOS) as the silica precursor material and boehmite (AlO(OH)) sol as the Al_2O_3 precursor. The composite powder, called M32, is base-catalyzed to produce discrete particles and because there is no interest in forming a ceramic monolith, only the coated particles, the synthesis time is greatly reduced; ageing times of many hours are often required for formation of a gel network [66].
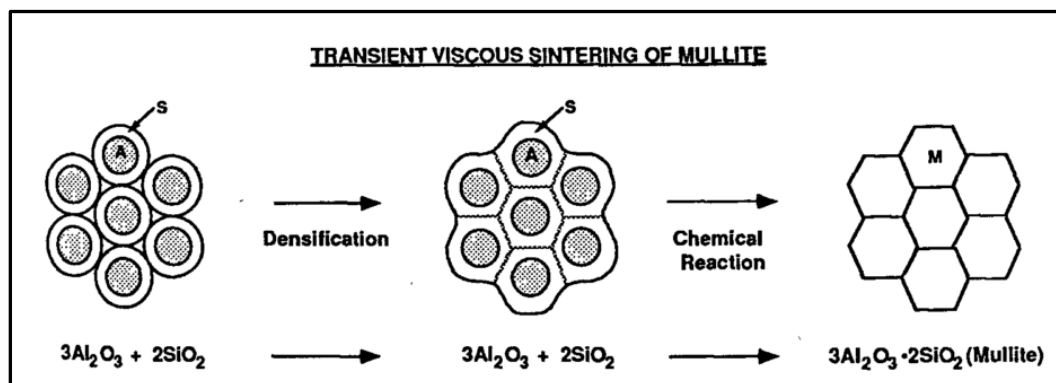
Figure 2.2. Diagram depicting the synthesis of premullite and reaction to 3:2 mullite.

For the *in situ* synthesis of mullite in a functionally graded composite application, alumina and an aluminosilicate may be used, such as kaolin. When designing an alumina to mullite gradient, it is assumed that as the ratio of alumina:kaolin changes from the ratio necessary to form mullite, a resultant phase will be a mixture containing a solid solution of mullite with precipitated Al_2O_3 as the gradient increases in Al_2O_3 content. This is shown in the Al_2O_3- SiO_2 binary phase diagram Figure 2.3, as the mol% Al_2O_3 increases within approx. 58-65%, the mullite solid solution forms. Traditionally, mullite synthesis requires sintering above 1600°C with multiple hour hold times (> 5 hr) to yield dense mullite. Sintering aids or "mineralizers," such as CaO, MgO, CeO_2 etc., may be used to facilitate lower sintering temperatures due to the formation of a glass phase that decreases diffusion time for densification and grain growth; the limiting factor to densification is diffusion of Si^{4+} [67], [68].

2.4.3 3 mol% Yttria-Stabilized Zirconia. Pure zirconia, without a stabilizing agent, is not a viable option for fabrication of single-phase zirconia parts, due to high temperature phase transformations. Upon cooling, the crystal structure will transform from tetragonal to monoclinic at 1200°C, which is the low temperature martensitic (t-m) transformation, which results in a 3-5% volume expansion [69]. This expansion in the matrix of a sintered bulk leads to catastrophic fracture of the ceramic body. To stabilize

the high temperature phases and prevent transformation upon cooling, soluble oxide stabilizing agents are added, such as yttrium oxide, also called yttria (Y_2O_3).
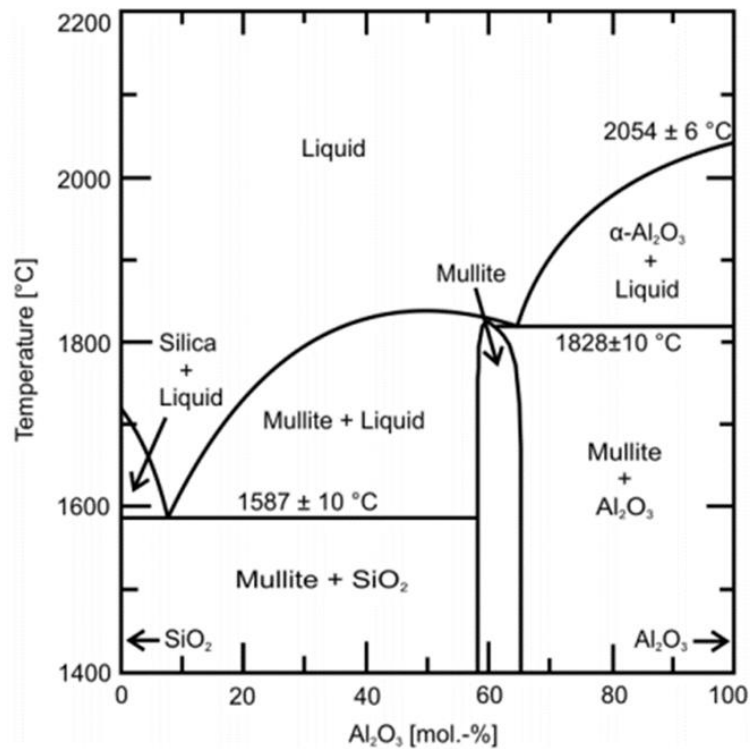
Figure 2.3. Al_2O_3-SiO_2 phase field showing solid solution formation at approx. 58-65% alumina content. This solid solution phase is called mullite.

Doped zirconia is analogous to pure zirconia, but the dopant ions, e.g. Y^{3+}, sit on the Zr^{4+} sites, and charge is maintained by partial oxygen site vacancy. Stabilization occurs due to intra-granular precipitations of tetragonal zirconia, though metastability can occur when the tetragonal precipitates are too small and do not transform or are too large and spontaneously transform to the monoclinic crystallographic arrangement [70]. For the purpose of this study and interest in tough technical ceramic composites, the 3 mol% yttria-stabilized zirconia system was used to develop a high solids loading paste.

3. REACTION SINTERING ZIRCONIUM DIBORIDE BY OXY-CARBO-NITRIDE SYSTEM FOR CERAMIC ON-DEMAND EXTRUSION

3.1. PROJECT INTRODUCTION

Most additive manufacturing techniques, including stereolithography, have difficulties fabricating ultra-high temperature ceramics (UHTCs) and non-oxide materials. This is due to nonmetals, metals, and metalloids' ability to absorb or reflect the light used to initiate photopolymerization, resulting in partial or incomplete polymerization. Ultimately, the result is poor resolution, insufficient cure depth, or unacceptable structural integrity. A system was devised using reactant materials that would act as discrete pastes but be mixed to the appropriate ratio using CODE to result in a zirconium diboride bulk. The system would then require further development as a four-phase system (oxide, carbide, nitride, resin) for stereolithography, with a resin refractive index near that of one of the reactants [71]. Zirconium oxide was chosen as the zirconium source and boron nitride as the boron source, rather than boron oxide, to prevent the liquefaction and volatilization of the boria during the reaction process. Boron nitride acts as both boron source and high temperature reducing agent. To verify pressureless sintering and reaction route a carbon source was included, using boron carbide, to increase the reduction potential and boron content.

3.2. EXPERIMENTAL PROCEDURE

The surface area of as-received powder was measured using nitrogen adsorption analysis according to the Brunauer-Emmett-Teller method (BET), (Nova2000e, Quantachrome Instruments, Boynton Beach, Florida, USA) and the particle size distribution by laser diffraction (S3500, Microtrac, York, Pennsylvania, USA). Sedimentation studies were used to approximate the best concentration of dispersant on a surface area basis, using Darvan C-N (ammonium polymethacrylate; Vanderbilt Minerals, LLC, Norwalk, Virginia, USA) and Dolapix CE 64 (carbonic acid; Zschimmer & Schwarz, Lahnstein, Rhineland-Palantinate, Germany). For a sedimentation study, 0.5-2.0 mg/m^2 dispersant was added to respective 10 mL graduated cylinders with pH 10.0 solution with 3 g of as-received powder. Each cylinder was covered using paraffin film,

agitated, then ultrasonicated for 600 s before being left stationary for sedimentation. The levels of sediment were monitored every 30 min for 8 hr and repeated for 1 g samples. The pH value was measured using a pH meter (HI 2210, Hannah Instruments, Woonsocket, Rhode Island, USA) and adjusted dropwise using an ammonium hydroxide solution (NH_4OH, 30% NH_3 basis, Sigma Aldrich, St. Louis, Missouri, USA).

3.2.1 Pressureless Sintering. Commercially available zirconium diboride (ZrB_2, Grade B, H.C. Starck, Karlsruhe, Baden-Wüttemberg, Germany) and boron carbide (B_4C, Grade HS, H.C. Starck, Karlsruhe, Baden-Wüttemberg, Germany) powder were used to establish a baseline sintering temperature. The reported average particle size was in a range of 1.5-3.0 µm with a 97% (metal basis) purity for ZrB_2; the average particle size of the B_4C powder was 0.8 µm, with a surface area of 15-20 m^2/g, and a B:C ratio of 3.7-3.8. A ZrB_2 composition with 4 wt% B_4C additive was used for pressureless sintering studies. These powders were attrition-milled in a polymer-lined jar using cobalt-bonded tungsten carbide (WC) media at 600 rpm for 2 h in acetone or methyl ethyl ketone (MEK, Sigma Aldrich, St. Louis, Missouri, USA).

After milling, the powder was retrieved via rotary evaporation (Rotovapor R-124, Bucchi, Flawil, St. Gallen, Switzerland). The powder was then crushed using a diamonite mortar and pestle and passed through a sieve stack: 250 µm / 60 mesh; 150 µm / 100 mesh; 106 µm / 140 mesh; and 90 µm / 170 mesh. Collected powder was uniaxially pressed into pellets for a sintering study. Two samples, of five pellets each, were made using a laboratory benchtop press (model 3851-O, Carver, Wabash, Indiana, USA), one set with and the other without a high molecular weight polyvinyl alcohol binder (PVA; avg. molecular weight 70,000-100,000, Sigma Aldrich, St. Louis, Missouri, USA). Due to incompatibility between PVA and MEK, batches that included binder were milled in acetone. After the doped ZrB_2 powder was retrieved, PVA binder was introduced as a 10 wt% solution resulting in 0.1% binder and the mixture was milled in a high density polyethylene (HDPE) wide-mouth bottle with WC media for 2 h to homogenize. Solvent was removed by boiling the slurry under a high (700-1200) rpm stir until dry, rather than rotary evaporation to prevent low recovery. For each pellet, 1.5 g of powder was loaded

into a 12.7 mm die and pressed for 60 s at 70.3 MPa; between pellets, the die was cleaned with acetone and lubricated with stearic acid.

The samples were sintered individually; a 6.35 cm dia. x 5.33 cm tall cylindrical graphite crucible was lined with flexible graphite foil (GRAFOIL, GrafTech Intl., Parma, Ohio, USA) and coated with an aerosol boron nitride lubricant (BN SP-2018, Materion, Buffalo, New York, USA) for sintering. Once dry, the crucible was loaded and topped with a permeable graphite foil lid. The sintering schedule was carried out in a resistance-heated, graphite, bottom-loading furnace (model 1000-4360-FP30, Thermal Technology Inc., Santa Rosa, CA, USA). The furnace was ramped from room temperature to $700^{\circ}C$ at $10^{\circ}C/min$ in flowing argon. Once at temperature, the furnace was held for 0.5 h before ramping to $1450^{\circ}C$ at $10^{\circ}C/min$. A partial vacuum (~160-120 millitorr) was pulled and the temperature held for 1 h. Afterward, the furnace was ramped to $1600^{\circ}C$ at $10^{\circ}C/min$ and held for 1 h. During these high temperature isothermal holds, the mild vacuum was monitored; an increase in pressure indicated volatilization of material or that reaction was occurring. A manual hold, not exceeding an additional 15 min, was performed to allow the vacuum to decrease as much as possible before proceeding. The final ramp from $1600^{\circ}C$ to $1900^{\circ}C$ at $30^{\circ}C/min$ occurred under flowing argon, then dwelled for 2h to sinter, and cooled to $50^{\circ}C$ at a rate of $30^{\circ}C/min$.

Relative density of each sample was determined using the Archimedes' method with water as the immersion medium. All pellets were weighed to obtain their dry mass, D, put in individual beakers of distilled water, and brought to a boil. Then the beakers were transferred to a vacuum chamber, where they were infiltrated for 24 h. The vacuum was checked and re-pulled at 10 h to ensure integrity. After the saturated weight, M, and suspended weight, S, were measured and the bulk density was calculated according to Equation 3 [72]:

$$B = D/(M-S) \hspace{3cm} (3)$$

Percent relative density was then determined by dividing the bulk density, *B*, by theoretical density. The value of the theoretical density of a mixed powder was determined by a rule of mixtures calculation.

Specimens achieving higher than 98% theoretical density were then mounted to polish the face of the pellet to a 0.25 μm finish using successively finer diamond abrasives. The specimens were chemically etched in a 1:1 KOH solution at 200°C for 30 s; their microstructures were analyzed using scanning electron microscopy (SEM; field emission S-4700, Hitachi, Schaumburg, Illinois, USA). An average grain size was measured using ImageJ, the open source imaging software (National Institutes of Health, Bethesda, Maryland, USA).

3.2.2 Reaction Sintering of ZrB$_2$. The sequence of reactions in Table 3.1 was the assumed route of reaction for *in situ* reaction sintering. Reactions (2) - (5) represent sequential and concurrent reactions, while reaction (1) is the intended overall reaction. The Gibbs free energy (ΔG) values can be calculated using: $\Delta G = \Delta G^{o} + RTlnK_p$, where ΔG^{o} is the change in standard state Gibbs free energy, *R* is the ideal gas constant, *T* is the temperature, and K_p is a reaction constant.

Table 3.1. Intended reaction path and Gibbs free energy for each reaction step.

Reaction	ΔG (kJ))
(1) $ZrO_2 + 2BN + 2C \rightarrow ZrB_2 + 2CO + N_2$	$\Delta G = 1055.6 - 0.761T$ ($\Delta G < 0$, T > 1115°C)
(2) $4BN + C \rightarrow B_4C + 2N_2$	$\Delta G = 941.0 - 0.487T$ ($\Delta G < 0$, T > 1659°C)
(3) $2ZrO_2 + B_4C + 3C \rightarrow 2ZrB_2 + 4CO$	$\Delta G = 1170.3 - 1.002T$ ($\Delta G < 0$, T > 895°C)
(4) $ZrO_2 + 3C \rightarrow ZrC + 2CO$	$\Delta G = 679.8 - 0.503T$ ($\Delta G < 0$, T > 1078°C)
(5) $ZrC + 2BN \rightarrow ZrB_2 + N_2 + C$	$\Delta G = 375.9 - 0.241T$ (Δ G < 0, T > 1287°C)

The reactants for reaction (1) were verified for nonstandard states at high temperatures for sintering and pressures below 1 bar, under flowing argon and partial

vacuum, using thermodynamic software, FactSage 7.0. Raw materials for reaction were commercially available zirconia (ZrO_2; Inframet Advanced Materials, Manchester, Connecticut, USA), boron nitride (BN; Grade F 15, H.C. Starck, Karlsruhe, Baden-Wüttemberg, Germany), and graphite (Carbon Black, Cabot, Alpharetta, Georgia, USA). A composition was batched according to the molar ratios of reaction (1) and mixed with WC media in a mill jar for 1 h in MEK. The solvent was removed via rotary evaporation and the powder uniaxially pressed according to the same procedure as the pressureless sintering study. These specimens were reaction sintered using the same rates and isothermal holds as the pressureless sintering study; this was to verify the times and temperatures for reaction. After reaction, the crystalline phases were identified using powder X-ray diffraction (XRD; PANalytical X'pert Phillips, Eindhoven, The Netherlands).

3.2.3 Extrudate Batching. Formulation of 55 vol% 10 mL test batches were done by mixing milled ZrB_2 + 4 wt% B_4C powders in 50 mL beakers using a flat stainless steel spatula. After achieving a smooth mixture, a binder solution was introduced, of which two types were used for the formulation of extrudate: PVA and cold water dispersible hydroxypropyl methylcellulose (Methocel J5MS, DOW, Midland, Michigan, USA). A baseline concentration of 1 wt% was used for PVA, while Methocel concentrations were 0.5 and 0.25 wt%. Rheometry was employed to measure the viscoelastic response of each extrudate batch.

3.2.4 Viscometry. A digital viscometer (DV-III, Brookfield AMETEK, Inc., Middleboro, Massachusetts, USA) was used for all viscosity measurements, with a small sample adapter and a number 28 spindle. With these peripherals, the possible viscosity range is 200-5,000,000 cP and the possible shear rate range is 0-56 s^{-1}. The chamber was loaded with 10 mL of extrudate, then the spindle was attached and inserted into the extrudate. Once the viscometer was loaded with a sample, a high shear history was put on the sample by running at 100 RPM for 5 min. Afterward, a viscosity reading was taken every 10 s for 180 s, after which the torque was recorded. This was repeated three times for each respective RPM, which was stepped 100, 75, 50, 25, and 5 to provide a range of shear stress.

3.3. RESULTS AND DISCUSSION

3.3.1 Verification of Pressureless Sintering. Two powders were investigated to confirm the efficacy of pressureless sintering a UHTC: ZrB_2 + 4 wt% B_4C and ZrB_2 + 4 wt% B_4C + PVA binder. Compact specimens of each composition were pressed at 70.3 MPa and sintered at 1900°C with a 2 hr hold. Pellets pressed without a binder had an average green density 59% and sintered to 79.6% of theoretical density indicating negligible densification. Specimens containing PVA binder had an average green density of 61% and sintered to near theoretical density (≥99%). Microstructural analysis was done to measure the average grain size and verify the sintering schedule of pressurelessly sintered ZrB_2 + 4 wt% B_4C. As shown in Figure 3.1, there is no intergranular or intragranular porosity, which verifies the sintering time and temperature to achieve high relative density. In the high magnification image (a), it is possible to see some voids, but this is due to polishing and the caustic nature of the KOH etchant, not a product of sintering. A grain size analysis was done using ImageJ to measure the average grain area and estimate an equivalent circular diameter. Using this method, the approximate grain diameter of the specimens sintered at 1900°C was 10.56 µm, based on a count of 797 grains. This included only the grey phase, in Figure 3.1, which is ZrB_2, while the black phase is B_4C.

3.3.2 Preparation of Single-Phase Paste. Dispersions with Darvan C-N and Dolapix CE 64 all suggest 0.5 wt% Darvan C-N to be most effective at dispersing submicron ZrB_2 powder in an alkaline pH≈10 suspension. Dispersions were checked every 30 min and most of these rapidly sedimented, leaving a clear or nearly transparent supernatant fluid after 1 hr. The accuracy of this test is in question without zeta potential measurements to verify the dispersion stability; however, it is known that the isoelectric point of ZrB_2 is pH ~ 4.5 according to studies done by Huang (2007) [73], and that an alkaline pH > 8.0 will provide maximum stability. Huang et al. (2007) did a similar study and fabricated a high solids loading ZrB_2 paste using the dispersant Darvan 821A (ammonium polyacrylate). They noted that Darvan 821A shifted the IEP to a pH 1.8, while ammonium polymethacrylate dispersants (Darvan C) shifted the IEP to a slightly higher pH 2.7. In the study, both Darvan C and Darvan 821A exhibited an IEP near pH
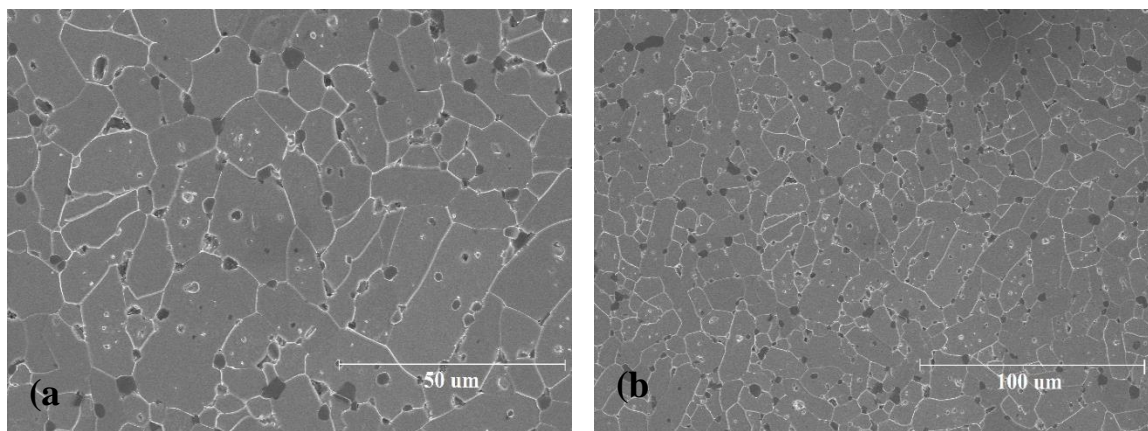
Figure 3.1. Microstructure of pressurelessly sintered ZrB$_2$; (a) high magnification showing no inter- or intragranular porosity; (b) low magnification, showing grain development and pinning.

9.0, but Darvan 821A had a zeta potential near -110 mV, while Darvan C exhibited a zeta potential of only -50 mV. The zeta potential of Darvan C is similar to that of the zeta potential of solution of ZrB$_2$ particles in water, suggesting that ammonium polymethacrylate is not effective at dispersing ZrB$_2$, especially compared to Darvan 81A [74]. However, zeta potential measurements are performed at low concentrations when the particle-particle interaction is the least, and more of a measure of particle-medium interaction. Such measurements are good initial steps for system design, but for high solids loading, dynamic approaches such as rheology are a better quality control metric for stability. Powders used for dispersion were characterized with surface area and particle size analysis, the results of which are listed in Table 3.2.

Viscometry of the high solids loading test batches with PVA and Methocel binders showed a strong non-Newtonian relationship for batches with 1 wt% PVA and 0.5 wt% Methocel (Figure 3.2). The trend of decreasing viscosity with increasing shear rates is the hallmark of non-Newtonian response, i.e. shear thinning.

Table 3.2. Measured physical properties of powders.

Material	Surface Area (m²/g)	Average Particle Size, d_{50} (μm)
Boron Carbide (B₄C)	16.653	0.82
Boron Nitride (BN)	9.931	-
Graphite I	30.172	-
Zirconia (ZrO₂)	15.467	0.53
Zirconium Diboride (ZrB₂)	1.849	2.58

One batch of 1 wt% PVA was tested 24 hr after batching, to determine the effect of sedimentation and current extrudate shelf-life. At the lowest shear rates, the drag on the spring-spindle assembly reached the maximum torque; similar behavior was seen with low concentrations of Methocel. This response in the sedimented PVA batch was due to high shear stress from friction between the sediment. The batch with low concentrations of Methocel may have exhibited similar behavior, but due to the molecular weight of the binder (86,000 g/mol) and likely bridging between adsorbed species. Higher concentrations of binder exceeded the maximum viscosity of the viscometer, while lower concentrations did not provide consistent data, trial to trial, across the entire shear stress range, suggesting more sensitive measuring equipment is required.

Wiesner et al. (2016) used highly-loaded, $\varphi=49$, ZrB₂ suspension for injection molding experiments. Their tests similarly suggested that the higher binder content increased the stress required to initiate flow. The binder used was polyvinylpyrrolidone (PVP) in concentrations as high as 5 vol%, while the lowest stress to initiate flow was measured at concentrations of 3 vol% [75]. Similarly, when the concentration of Methocel was halved, the data was more consistent, less shear thinning, and lower torque. The lower stress was likely due to improved steric stabilization and adlayer thickness from an appropriate concentration of binder.
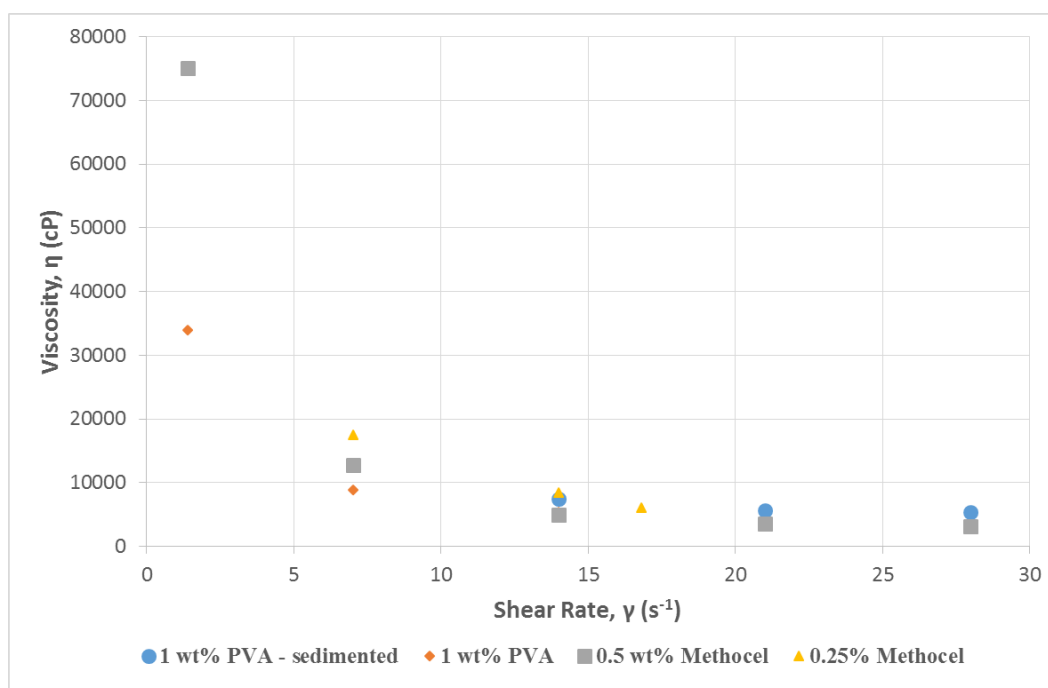
Figure 3.2. Comparison of PVA and Methocel binders in high solids loading batches of single phase ZrB$_2$ paste.

Based on the rheological measurements, a 55 vol% sample batch of extrudate was made using 0.5 wt% Methocel to print test bars via CODE. A-bar geometries (2.0 mm x 1.5 mm x 25 mm), according to ASTM C1161-18 *Standard Test Method for Flexural Strength of Advanced Ceramics at Ambient Temperature* were fabricated for a sintering study [76]. Unfortunately, as seen in Figure 3.3 post sintering longitudinal cracks were seen in all bars along the entire length and through the thickness. Not visible after drying, they were however due to drying stresses and became exaggerated during the sintering process. The fractures appear to follow the fusion lines between rasters and are able to run along the thickness because of how the rasters aligned during deposition. Not until the rasters are slightly misaligned does the fracture diverge and terminate. Fracture behavior like this is known to follow the weakest barrier and is a perfect example of designing for additive manufacturing and the effect of aligned rasters in a fabricated specimen. The density of these specimens was not recorded, due to the critical fracture.

Many studies have been applied to the change in mechanical properties according to print orientation of polymers. Feilden et al, (2017) studied hierarchical design of bioinspired ceramic materials to control crack propagation. As expected, trans-filament flexural strength of their Al_2O_3 structures exhibited the highest values, 202 ± 10 MPa, while the traverse filament flexural strength exhibited the lowest at 125 ± 12 MPa with fracture propagating along the aligned raster boundaries [77]. The same failure mechanism is proposed in Figure 3.3, though exacerbated due to the low relative sintered density.
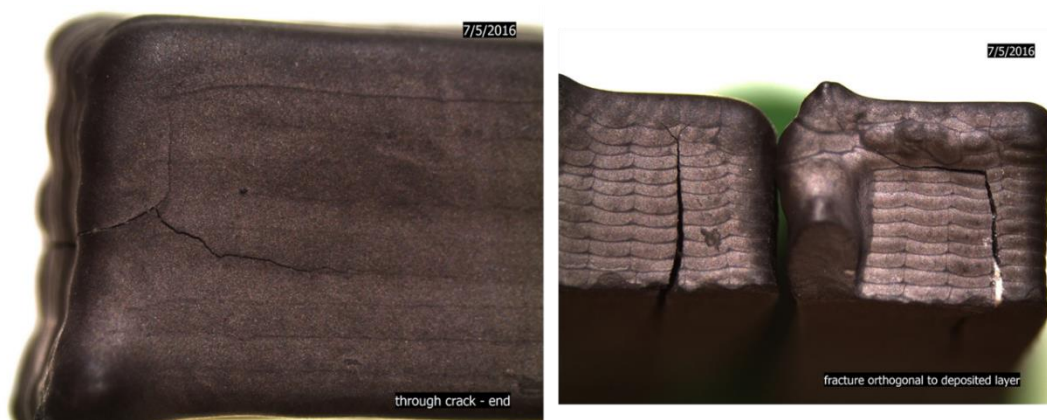
Figure 3.3. Transverse through-cracks in CODE ZrB_2 specimens following aligned inter-raster bonding locations.

3.3.3 Reaction Sintered ZrB_2. Without the ability to characterize the paste fully, single-phase paste was abandoned in favor of characterizing the reaction-sintered system. A reaction to yield ZrB_2 is often the decomposition of a boron species (borothermal) or carbon species (carbothermal) with a zirconium source. The oxide-carbide-nitride system proposed is a hybrid boro/carbothermal reduction. This multi-step reaction (Table 3.1) was verified by thermochemical software, however the path may be affected or hindered by particle size, the isothermal holds during sintering, and partial vacuum steps during sintering. For this reason, powder XRD analysis of crushed samples was used to identify
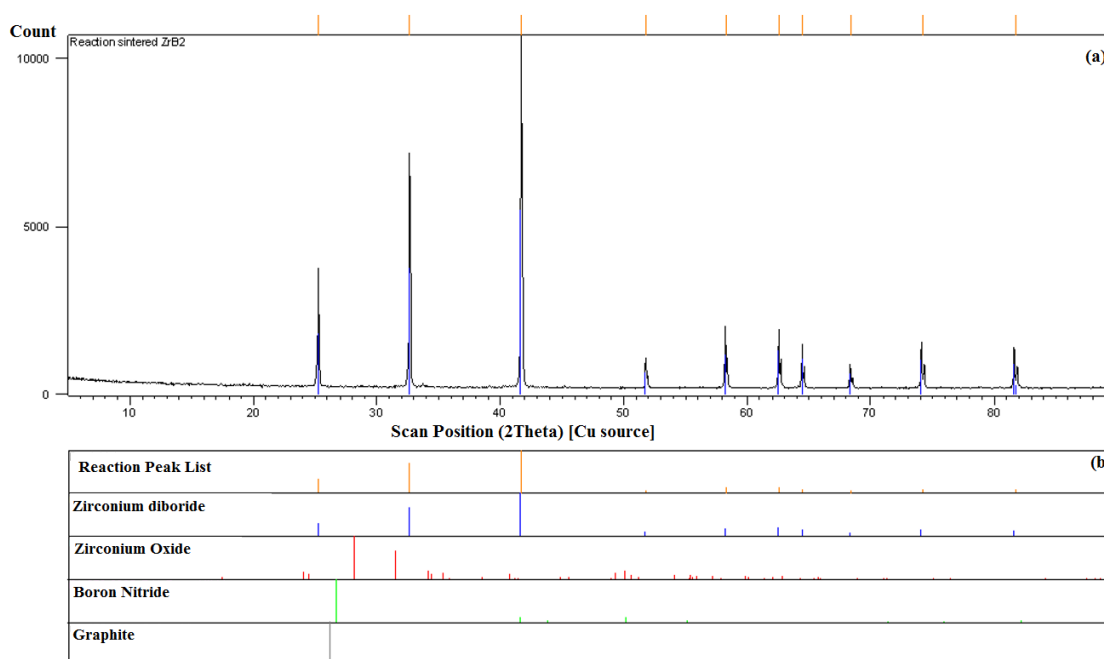
Figure 3.4. XRD micrograph of predominant phase of reaction sintered ZrB$_2$ showing single phase, crystalline ZrB$_2$ through hybrid boro/carbothermal reaction.

the product, revealing that the predominant crystallographic phase of the powder sample was zirconium diboride (Figure 3.4a). Residual phases from incomplete reaction would present themselves as intermediate intensity peaks, such that peaks in Figure 3.4a. However, this is not the case, as the peaks of the scanned sample correspond to the chemical tag of zirconium diboride. None of the major peaks of the reactants present themselves, confirming the formation of single phase crystalline zirconium diboride. Unfortunately, because of the starting materials: ZrO$_2$, BN, and C, the nominal volume change of the system was 40.5% resulting in a relative density of 74% when sintered at 1950°C for 2 hr.

In terms of reaction sequence, this chemistry is viable for forming ZrB$_2$ *in situ*, but without further analysis of sintering agents, temperature, and time, this system is inviable for pressurelessly fabricating functional ZrB$_2$ parts with CODE. In Guo and Zhang (2009), the reaction route of boro/carbothermal reduction of ZrO$_2$ to produce ZrB$_2$ was analyzed. Using B$_4$C as a reducing agent with carbon, they considered the reactions:

$$2ZrO_2 + B_4C + 3C \rightarrow 2ZrB_2 + 4CO \tag{4}$$

$$7ZrO_2 + 5B_4C \rightarrow 7ZrB_2 + 3B_2O_3 + 5CO \tag{5}$$

$$ZrO_2 + B_2O_3 + 5C \rightarrow ZrB_2 + 5CO \tag{6}$$
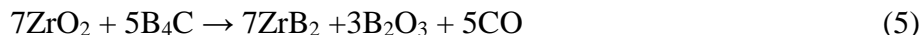
when in standard state ($P_{co} = 1.013$ bar), the reaction in equations 4-6 above become thermodynamically favorable at 1424°C, 1218°C, and 1509°C respectively. Using this reaction path, it is assumed that the zirconia will be continuously reduced by B_4C and C additions, further reaction with formed B_2O_3 until no oxide phase remains and producing only ZrB_2 and carbon monoxide. Their analysis was of synthesized powder, not a powder compact, so no density information is available, but they did note the difference in powder morphology dependent on sintering temperature: columnar at 1750°C and spherical at 1650°C [78][77].

An intermediate phase that could possibly form, not reported in Guo and Zhang (2009), is zirconium carbide (ZrC) from the reaction of $ZrO_2 + C$. Another publication on the study of *in situ* synthesis of SiBCN-Zr, outlines the reaction of ZrO_2 with boron nitride (BN). This reactant will act as a high temperature reducing agent as well as a boron source for reacting ZrB_2 favorably. Miao et al. stated that not only does BN reduce ZrC, but also ZrO_2, aiding in the prevention of oxidation at temperatures above 1600°C [79].

The proposed reaction path in Table 3.1: $ZrO_2 + 2BN + 2C \rightarrow ZrB_2 + 2CO + N_2$, is corroborated by Guo and Zhang (2009) and Miao et al. (2016), so this path was chosen from a similar study by Yan et al. (2016) [80]. Their thermodynamic and XRD analyses suggested that the overall reaction became thermodynamically favorable at temperatures $< 1200^o$C and could synthesize submicron powder (200-800 nm) at temperatures as low as 1550°C. The BN and C reactants would continue to act as reducing agents at temperatures above 1200°C to reduce ZrC and form B_4C, which was the low temperature reducing agent for ZrO_2. This reaction path produced non-oxide ceramic phases, and reduced intermediate reaction phases, along the entire heat treatment to 1550°C, making it favorable for low temperature *in situ* synthesis. However, much higher temperatures, 1900°C and above, were necessary for densification.

4. DEVELOPMENT OF A 3YSZ PASTE FOR CERAMIC ON-DEMAND EXTRUSION

4.1. PROJECT INTRODUCTION

With the development of CODE and its establishment as a viable extrusion AM technique, several iterations of test pastes were produced to begin the fabrication of complex parts with embedded components. The proof-of-concept paste for the use of zirconia was a fully stabilized, 8 mol% yttria-stabilized zirconia system. This paste was used to fabricate rectangular bulk specimens for mechanical testing, which is described fully in [81]. With the success of the stabilization of a zirconia paste, a similar strategy was applied for the 3YSZ paste system, which was used with both inorganic [82] and organic [83] support materials to fabricate increasingly complex components. The inorganic support material being a high solids loading calcium carbonate ($CaCO_3$) paste, necessitating a two-step sintering processing, with intermediate dissolution of the evolved calcium oxide (CaO). The process for formulating this support material paste is not expanded upon here.

4.2. EXPERIMENTAL PROCEDURE

4.2.1 Determining Stability. Prior to performing sedimentation tests, the surface area of the as-received TZ-3Y-E powder was measured by nitrogen adsorption analysis using the Nova2000e. Two dispersants were selected, Dispex CX 4240 (ammonium polyacrylate, BASF Corporation, Cleveland, OH, USA) and Dolapix CE 64 (ammonium polyacrylate, Zschimmer & Schwarz, Inc., Lahnstein, Rhineland-Palatinate, Germany) for sedimentation studies. Two settling studies were performed to identify the pH and concentration for stability. To identify an appropriate concentration, ten graduated cylinders were filled with a pH 7.0 solution to test the effect of dispersant concentration. The concentrations were measured according to powder surface area, from 0.2-2.0 mg/m^2. Ultimately the concentration was determined to be approximately equivalent to 5 wt% (dry weight basis) of the dispersed phase.

The concentration was then kept constant at 5 wt% and the pH adjusted to determine the effect of pH on dispersion stability. Ten graduated cylinders were filled

with pH adjusted solution from pH 1-10 respectively and 1 g of TZ-3Y-E (3 mol% yttria-stabilized zirconia, TOSOH, Grove City, OH, USA); the pH was adjusted using either hydrochloric acid (HCl) or ammonium hydroxide (NH_4OH). Dispersion stability was determined by qualitatively measuring the separation of the opaque and supernatant fluids within the graduated cylinders, i.e. the level of the opaque liquid, supernatant, and type (hard or soft) of sediment after 18-20 hr.

4.2.2 Paste Production. Paste was produced in batches 24 hours prior to fabrication, according to need. Batches were produced in 50-100 mL quantities and consisted of 50 vol% ceramic solids. Ammoniated water was prepared using distilled water and 30% ammonium hydroxide solution (NH_4OH, Sigma Aldrich, St. Louis, MO, USA). The pH was adjusted until an alkaline pH $\approx$ 9-10 was achieved, as measured by a pH meter (HI 2210, Hannah Instruments, Woonsocket, RI, USA). Dolapix CE 64 was used as the dispersant and no binder was used. The paste was milled in a HDPE jar using spherical 3mm zirconia grinding media (YSZ, Inframat Advanced Materials LLC, Manchester, CT, USA) for 18 hr to homogenize. Post recovery deaeration was done using a vacuum power whip mixer (Model F, Whip Mix, Louisville, KY, USA), pulling a mild vacuum (~20 kPa). The final step involved transferring the paste to charging syringes, that attached to the CODE auger valve, which were agitated on a vibratory table to remove entrapped air.

4.3. RESULTS AND DISCUSSION

4.3.1 Paste Performance. The measured surface area of the TZ-3Y-E specimen from lot #S300894P was 6.002 m^2/g with a correlation coefficient value $r = 0.99991$, suggesting little data scatter and near linearity. Using the surface area to determine the concentrations of dispersant Dispex CX 4240, concentrations were tested from 0.2-2.0 mg/m^2 using 1 g of zirconia powder mixed into each respective graduated cylinder filled with pH 7.0 solution. The graduated cylinders were monitored for four hours, noting the level of sedimentation of each on the hour. Except for extreme pH's 1.0, 9.0, and 10.0, Dispex CX 4240 proved ineffective to disperse TZ-3Y-E. The same experiment was repeated with Dolapix CE 64, with similar results – no dispersion at pH 7.0 and full

sedimentation after 1 hr for the majority of the sample. The pH_{IEP} of the 3YSZ is approximately pH 4.5-6.0, so it was expected that the colloid could be dispersed using an ammonium polyacrylate in the acidic regime, however Y^{3+} leaches into acidic solutions.

Sedimentation at a neutral pH was not unexpected, as a neutral pH is above the pH_{IEP} for 3YSZ so the surface is nominally negative and both Dispex and Dolapix are anionic dispersants. The trials were repeated with increasing concentration of dispersant until it was determined that Dolapix CE 64 provided stability in both extremes of pH with an optimal concentration of 8 mg/m^2, which was approximately equivalent to 5 wt% on a dry weights basis of the zirconia powder with a surface area of 6.016 m^2/g. The dispersion mechanism was assumed to be electrosteric for the acidic regime, and deleption stabilization for the alkaline regime. With a high solids loading $\varphi > 0.5$, depletion stabilization was a better option for attempting to design shear thinning behavior without rheological measurements. Using an acidic pH would have initially provided the highest stability for the paste because of strong adsorption of the dispersant. However, it would have limited dispersion stability (shelf life) because of the leaching Y^{3+} in solution, which would destabilize the paste over time.

In contrast, the dispersant acted as a depletant in solution of alkaline pH, by only adsorbing to some surface sites in low concentration. This high pH would also cause the species to experience full hydration and intersegment repulsion, so the dispersant would take up the maximum volume and creating a larger double layer, σ, between particles. Resulting shear thinning behavior seen in the paste was then the result of the concentration and conformation of the depletant, which was flocculating $\leftrightarrow$ restabilizing the suspension.

Non-idealized dispersion conditions were chosen by controlling ΔpH such that the suspension was above but near the boundary of the pH_{IEP}. At the boundary of the suspension pH_{IEP} there will be localized instability introduced and particles will begin to weakly flocculate. A designed extrudate in this fashion will act as a bulk solid until a stress is applied, upon which the viscosity decreases and the paste flows readily. After deposition the applied stress is effectively removed and the bulk behavior becomes solid again. This occurs due to shear stresses from the auger valve or slip from pneumatic

pressure at the chamber wall, which can readily separate the weakly flocculated particles, disrupting the percolated network. Once separate and locally dispersed, the viscosity decreases sharply.

Analysis of the surface chemistry of zirconia polymorphs by Hertl [81], suggests that thermal treatment of zirconia has a drastic effect on the surface chemistry. Tetragonal zirconia readily acts as a Lewis acid, with site charges of 2+. Reaction with CO or carbonates in solution readily produce carbonic acid, HCO_3^-, which would suggest the need for a strong stabilizing counter ion and adsorbate to disperse zirconia. Recent studies show the effect of counter and co-ions on the stability of colloids. Cao et al. related the ionic strength of co-ions, those with the same charge as the surface, and counter-ions in solution to a critical concentration at which irreversible flocculation occurs [85]. Ultimately, they determined that regardless of the species, organic or salt, the critical concentration scales with the inverse of the valency of multi-valent species. This is further verification of the application of depletion stabilization mechanisms, not only effective for dispersion, but also stabilization of the pH.

Two other studies also discussed the network of concentration nanoparticle suspensions, and the effect of stability on structure and fluid properties. Rao [86] and Conrad et al. [87] focused on establishing design criteria and a phase diagram for stability above or below the critical concentration point. They mentioned the effect of particle geometry on gel formation as concentration increases: particles are amenable to amorphous gels or crystals, while plates produce porous amorphous structures, and rods form aligned gel structures. The formation of the gel structure is highly susceptible to the surface chemistry and adsorbed species as one would expect, which explains the ability of spheres to form both crystals and glasses, rods to align, and platelets to only create porous networks.

The paste was qualitatively monitored batch-to-batch. With an assumed IEP, stability was designed around this using a pH > 9.0 and Dolapix CE 64. The effect of the solids loading and particle size are understood, but not quantitatively analyzed at this time. All parts fabricated with this paste were sintered at $1550^{o}C$ for 0.5 hr to achieve a submicron grain size. The initial sintering study compared sintering conditions of $1500^{o}C$

for 2.5 hr, 1500°C for 0.5 hr, and 1600°C for 0.5 hr. A microstructural analysis was performed using ImageJ software to measure the average grain area and estimate the equivalent circular diameter.

      4.3.2 Fabricated Demo Parts. Microstructures for the sintering study are shown in Figure 6.6., and though all reached a relative density > 95% they demonstrate the importance of optimizing the sintering schedule. The sample sintered at 1500°C for 2.5 hr exhibited an average grain size of 3.82 μm, based on a measurement of 304 grains; the sample sintered at 1500°C for 0.5 hr exhibited an average grain size of 0.63 μm; while the sample sintered at 1600°C for 0.5 hr exhibited an average grain size of 5.07 μm. This disparity between longer time or higher temperature shows that neither are a direct relation to densification. In the case of the sample shown in Figure 4.1a, the average grain size was 3.82 μm, while this is not large, there are some grains that are significantly larger than others. This, alongside the intragranular porosity indicates rapid grain growth, likely due to the sintering time. The sample shown in Figure 4.1b had the smallest average grain size, at 0.63 μm, it was sintered at a higher temperature than the sample in (A), but for a fifth of the time. The result is a submicron grain size, a uniform grain size, and no porosity. It is worth noting that the image in Figure 4.1B is of a free sintered surface because the sample was not polished to the same level as the samples in (A) and (C). Like the case of sample (A), the sample shown in Figure 4.1C exhibits a large average grain size at 5.07 μm and intragranular porosity. This is indicative that despite the time being the same as sample (B), the temperature was too high for sintering.

      The rheological properties of the 50-55 vol% pastes were consistent enough batch-to-batch that the system was deemed workable to fabricate dense, functional parts demonstrated in Figure 4.2. Further analysis was done on the mechanical properties of printed structures (see Li et al. [37]), spanning multiple publications, including a performance analysis of parts printed with organic support material and a similar analysis for dissolvable inorganic support material mentioned in the section 4 introduction.
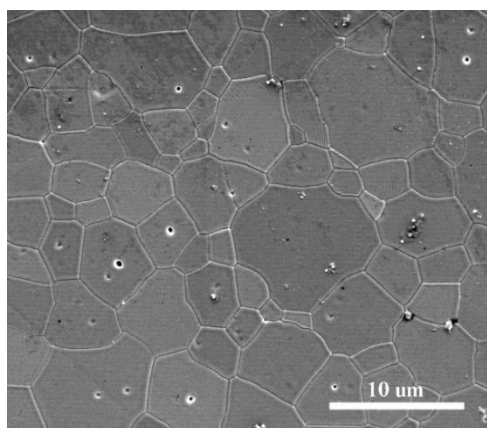
(A)
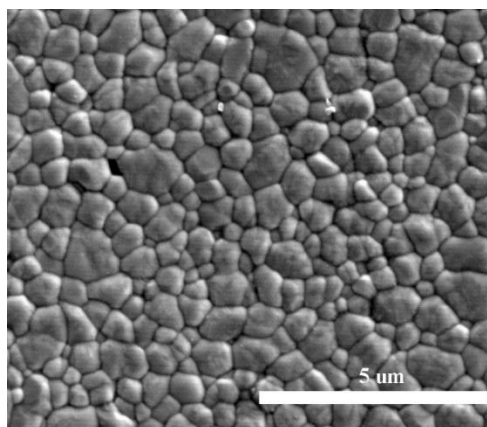
(B)
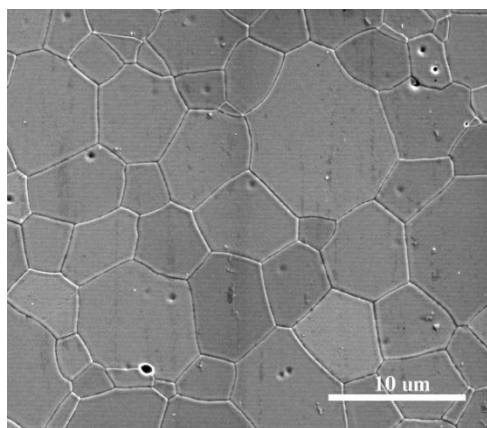
(C)

Figure 4.1. Microstructural development of 3YSZ under sintering conditions:
(A) 1500°C 2.5 hr, (B) 1550°C 0.5 hr, and (C) 1600°C 0.5 hr.
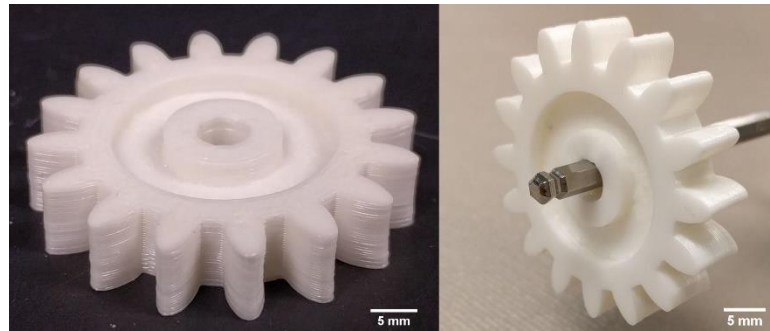
Figure 4.2. 3YSZ symmetrical gear fabricated via CODE.

To optimize the paste, it would be necessary to compare the effects of solids loading, dispersant, pH, and binder against the rheological response. An analysis would make it possible to control the extrusion behavior for more complex geometries, such as gap bridging and unsupported overhangs, as well as increase the solids loading by improving the suspension stability.

5. IDENTIFICATION OF ALTERNATIVE FABRICATION ROUTE FOR STOICHIOMETRIC MULLITE AT LOW TEMPERATURE AND SHORTENED SINTERING TIME

5.1. PROJECT INTRODUCTION

Another ceramic system needed to be identified for use in conjunction with alumina in a graded composite application. This system would be mixed in specific volume fractions as needed to create the alumina gradient, necessitating CTE and chemical compatibility. Mullite was chosen, not only because it is a well understood system, but also because it is the resultant solid solution of a specific ratio of alumina:silica. It was hypothesized that a gradient of alumina to mullite would be mechanically and chemically compatible due to the mixture of the solid solution and precipitated alumina phases, facilitating a functional gradient with favorable engineering properties. It was not known whether the co-sintering process would be detrimental to the alumina phase, due to mullite commonly being processed at temperatures exceeding 1600°C and isothermal holds exceeding 5 hours. The goal of the following study was to reduce the processing time and temperature of a theoretical alumina-mullite graded composite part.

Initial tests were performed to attempt to disperse and sinter stoichiometric mullite powder that was commercially available. It proved difficult to disperse and to require multi-hour isothermal holds for full mullite development. The surface area of these powders was measured after milling trials done at 18 and 20 hours to reduce their average particle size to a submicron range. Ultimately, it was determined that reaction sintering would be easier due to the readily available materials. Three methods were employed: reaction sintering of mullite and kyanite, reaction sintering of kaolin:alumina mixtures, and sol-derived premullite composite powders.

Six series of mullite, magnesium oxide, and kyanite were studied at sintering temperatures of 1550 and 1700°C to achieve densification. Magnesium oxide (MgO) was added at a constant concentration as a mineralizing agent, to pin grains and promote primary mullite formation. Kyanite was introduced at two levels of concentration for liquid phase sintering and mullite formation.

5.2. EXPERIMENTAL PROCEDURE

5.2.1 Reaction Sintering of Mullite via Kaolin-Alumina. For the fabrication of functionally gradient composites of alumina (Al_2O_3) and mullite ($3Al_2O_3 \cdot 2SiO_2$), the mixture of kaolin and alumina was studied at three sintering temperatures (1400, 1500, 1600°C) to yield stoichiometric mullite to alumina gradients. The ratio of kaolin-alumina to yield mullite is 2:2.68 kaolin to alumina, and so the sintering study was done to determine the lowest sintering temperature for dense, functional mullite without a sintering aid [88], [98].

Sintered specimens were crushed using a diamonite mortar and pestle and passed through a sieve stack: 106 µm / 140 mesh and 90 µm / 170 mesh, then analyzed via powder X-Ray diffraction (XRD) at room temperature using a powder diffractometer with Ni-filtered CuKα radiation (PANalytical X'Pert PRO, Malvern Panalytical, Westborough, MA, USA). Diffraction patterns were recorded in the 4° to 90° 2θ range, in continuous scan mode. Sintered specimens were polished to a 0.25 μm finish using diamond abrasive slurries and microstructural development was evaluated using SEM.

5.2.2 Synthesis of Stoichiometric Mullite via Sol-Gel Method. Despite successful formation and relatively high density of 90.8% for alumina-kaolin reaction-sintered specimens, an alternative route was investigated for the formation of mullite to decrease the sintering temperature and reduce the time required for thermal treatment. A composite premullite powder (M32) was synthesized using TEOS as the source of silica and boehmite as the source of alumina. The quantities of each were calculated to yield $3Al_2O_3 \cdot 2SiO_2$ once sintered. The tetraethyl orthosilicate (TEOS, Sigma Aldrich, St. Louis, MO, USA) was measured in a graduated cylinder, 30 mL total, then poured into a round bottom flask. This flask sat inside of a water bath that was held at 60°C. The stir bar was set to 40 RPM and 31 mL of ethanol was added. For base-catalyzed M32, 38 mL of ammoniated distilled water was poured into the flask. The pH must be ~9 for rapid hydrolysis, which required approximately 4 drops of NH_4OH.

Prior to mixing the ammoniated water and TEOS, a boehmite sol was prepared. A total of 72.1 g of boehmite (AlO(OH), Sasol, Westlake, LA, USA) was mixed into 300 mL of ammoniated water and allowed to mix using a magnetic stir bar for 10 minutes.

Once dispersed, this sol was then introduced into the TEOS/ethanol solution. The mixture was allowed to stir for 3 hr at 60°C to incubate, before being transferred to a large beaker and dried at 200°C in a convection oven. The powder cake was then collected and heat treated in a resistively heated muffle furnace (Vulcan 3-550, Bloomfield, CT, USA) to oxidize and form a silica layer. The cycle for oxidation was 2°C/min to 100°C with a 0.5 hr hold, ramp to 500°C at 5°C/min, hold for 5.0 hr, then ramp to 50°C at 10°C/min to complete. The M32 powder was pulverized using a diamonite mortar and pestle and passed through a sieve stack of 150, 106, and 75 μm, before being pressed into pellets using a polycarbonate binder (QPAC40, Empower Materials, Inc., New Castle, DE, USA) for a sintering study. Powder specimens were also used for differential thermal analysis (DTA) to measure the transformation of precursor materials at 1500°C, as well as phase development using XRD.

5.3. RESULTS AND DISCUSSION

Initial steps to formulate a 50 vol% paste out of single-phase mullite (MJ5M, Kyanite Mining Corp, Farmville, VA, USA), using Darvan C-N and Darvan 2 (Vanderbilt Minerals LLC, Norwalk, CT, USA) as the dispersant resulted in partial stability, with the high solids loading paste (55 vol%) slowly sedimenting, i.e. loss of 0.5-0.75 mL of liquid in 24 hr. The initial test batches were prepared at a pH 5.0, below the pH_{IEP} 7.0 of mullite. This partial stability was assumed to be due to low dispersant concentration, incorrect pH, and the lenticular geometry of mullite powder. This issue persisted after the powder was ball milled for 72 hr, resulting in a surface area of 4.831 m^2/g from 1.593 m^2/g in the as received state. The slow sedimentation was eventually prevented by introducing 1.5 wt% METHOCEL J7 MS-N solution (1 wt% solids) (hydroxypropyl methylcellulose, DOW Chemical Company, Florissant, MO, USA). With the addition of a binder, the suspension stability was over 48 hr, and a series of test bars were fabricated for sintering. Samples were sintered at 1550°C for 0.5 hr and 1700°C for 0.5 hr to compare sintering conditions similar to that of alumina and conditions that are necessary for mullite formation. The percent theoretical density of the sample sintered at 1550°C was 69.7%, while the 1700°C sample was 82.8%. Though there was significant

increase in density in the second sample, this temperature exceeds the sintering temperature that would be used for the systems combined with mullite in a composite, complicating the co-sintering process. It was believed that the >1550°C temperatures required for densification of mullite necessitated a lower temperature route if combined with Al_2O_3 in a graded composite.

The combination of aluminosilicates such as kaolin and alumina to form mullite are well known [88], [89], [90]. Three samples were mixed and pressed into pellets. A sample of five pellets was sintered for each temperature at 1400, 1500, and 1600°C respectively, each for 2 hr. Specimens showed residual alumina content when treated at 1400° and 1500°C for 2 hr, while the specimen sintered at 1600°C for 2 hr showed near complete reaction and dominant mullite formation, with unidentified peaks assumed to be residual alumina, shown in Appendix Figure 1 (Appendix Figure 1 is included in the Appendix for purpose of image clarity).

Though successful reaction occurred at modest temperatures in the range of 1400-1600°C, the specimens exhibited fracture during the sintering process; it is unknown whether this was due to mullite formation and phase expansion or was an artifact from sample preparation via compaction. The average relative density of the samples is outlined in Table 5.1, with the 1600°C sample achieving a relative density of 90.8%. Despite the ability of this sintering process to achieve final stage densification, it fails to achieve high relative density in a short time span, necessitating yet another method to form mullite that is > 95% theoretically dense.

Table 5.1. Relative density of sintered kaolin:alumina compacts for various sintering temperatures and a 2 hr isothermal hold.

Sintering Conditions [temperature ^{o}C (time hr)]	Relative Density (%)
1400 (2)	84.3
1500 (2)	84.8
1600 (2)	90.8

SEM micrographs in Figure 5.1 show the microstructural development of each specimen; the acicular grain morphology is indicative of mullite formation from reaction between kaolin:alumina. Some view microstructural development as a benefit for tough mullite, while it can also become a hindrance to full densification [91].
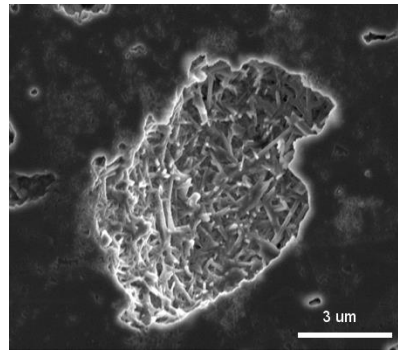
(A)
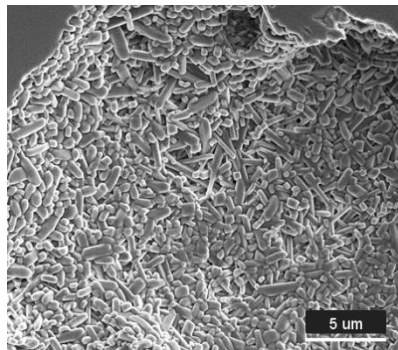
(B)
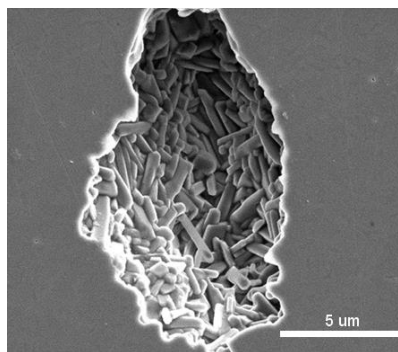
(C)

Figure 5.1. Microstructural development of (A) 1400ºC, (B) 1500ºC, (C) 1600ºC specimens sintered for 2 hours with acicular grains indicative of mullite formation.

The final attempt to develop a mullite system that would sinter at temperatures below 1600°C, after a single-phase paste and reaction sinter kaolin/alumina system, a diphasic mullite precursor was attempted. Several types of methods are available, such as monophasic, amorphous gels diphasic gels, or a hybrid mixture of polymeric gel and sol [92]. The synthesis of this premullite powder was fully described by Wei and Halloran [64] and could be synthesized in two ways: acid or base catalyzed. Batches of both types were synthesized and allowed to incubate in a water bath at 60°C to determine which yielded the highest surface area; this is outlined in Table 5.2.

There was not enough variance between the base and acid catalyzed series to suggest that incubation times would have an effect. However, acid catalyzed 48 hr incubation time yielded the highest surface area of all tested samples. For hybrid sol-gel methods, Huling and Messing (1989) suggest that incubation time may be critical, if a small polymeric gel fraction is included introduces potentially finer nucleation sites and increases the apparent rate for a finer grain size of 0.4 μm at 1550°C [93].

Table 5.2. Surface area of incubated acid and base catlayzed series M32.

Incubation time:	Acid Catalyzed	Base Catalyzed
	Surface Area (m^2/g) [correlation value, r]	
24 hr	N/A	**164.801** [0.9995]
48 hr	**206.413** [0.9966]	**165.194** [0.9995]
72 hr	**170.979** [0.9966]	**159.082** [0.9969]

A sample of acid catalyzed, 48 hr incubated M32 was analyzed using differential scanning calorimetry (DSC) (SDT Q600 Differential Scanning Calorimeter, TA Instruments, New Castle, DE, USA) to identify the characteristic exothermic peak around 1440°C, which suggests primary mullite formation. Figure 5.2 illustrates just that, with a sharp exotherm identified at 1442°C. This aligns with data collected in Schneider et al.
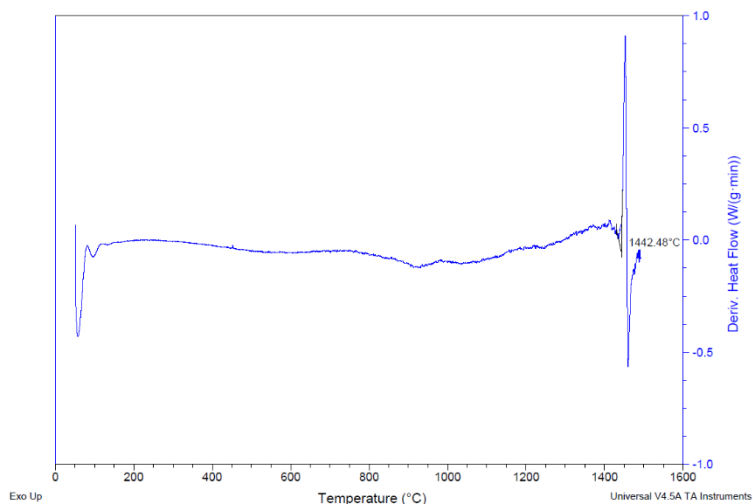
Figure 5.2. DSC micrograph showing premullite reactants converting to mullite according to characteristic mullite exotherm at 1440°C.

[94] as well as Wang and Sacks (1996) [95] for thermally treated diphasic mullite gels and represents mullite formation below 1550°C.

Three 25.4 mm diameter x 3 mm thick pellets were prepared for sintering. Incubated acid catalyzed series M32 was first mixed with 2 wt% QPAC40 and milled in acetone overnight. The sample was collected via rotary evaporation and passed through a 100 μm sieve. To consolidate the powder, 3.0 g of powder was pressed at 70.3 MPa for 60 s. These pellets were then sintered in a furnace (Deltech, Model 31-9, Denver, CO) at 1550°C for 1 hr; the cycle ramped to 750°C at 10°C/min, held for 0.5 hr, ramped to 1550°C at 5°C/min, held for 1 hr, and ramped to room temperature at 10°C/min to end. Unfortunately, the average relative density of these pellets was only 70.4% theoretical. However, there is some indication as to why in Figure 5.3. These curves represent the difference in energy required for mullite formation at the same heating conditions: 10°C/min to 1500°C. They indicated that when the M32 powder is milled the energy of formation required is significantly more endothermic than as-synthesized M32. This suggests that the intimate contact of the Al_2O_3 and SiO_2 formed during synthesis and oxidation is completely undone by milling the powder for 18 hr.
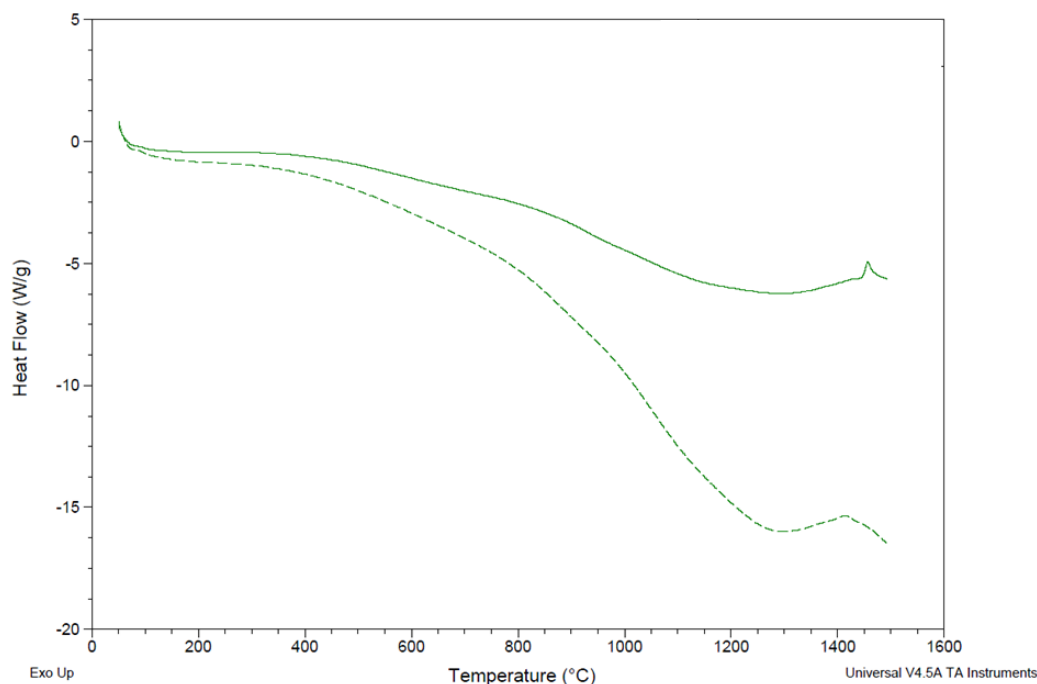
Figure 5.3. Heat flow of as-synthesized (top) vs. milled (bottom) M32, with evident increase in energy requirements to convert premullite powder to mullite due to separate of reactants after milling process.

No pellets were sintered of as-synthesized powder, though it is hypothesized that it will form mullite. Analysis by Wei and Halloran identifies that stoichiometric aluminosilicate gels, like the ones produced, can produce mullite at modest temperatures. However, formation and densification are controlled by short-range diffusion and transformation is preceded by a temperature-dependent incubation time [96]. This confirms that though mullitization can occur at temperatures below 1300°C, isothermal treatment cannot be avoided for full development, only reduction of the temperature at which it is necessary. In this study, that was avoided to prevent complications with future alumina:mullite graded composites, for fear of exaggerated grain growth in the alumina. Wei and Halloran also proved through direct microstructural observations that growing mullite phase in diphasic gels pins larger Al_2O_3 grains. This mechanism may be the key to prevent previous fears for processing a mullite:alumina graded composite.

A later analysis by Sacks et al. (1991) also confirmed the analysis by Wei and Halloran, finding that full densification can occur as low as 1300°C with multi-hour isothermal holds to develop fine grained mullite at higher temperatures of 1550°C [98]. With this evidence from the literature, it is clear that a study should be conducted to determine an improved method for reduction of the sol-gel processed M32, a design of experiments to control the average particle size of synthesized composite powders, or direct fabrication using the gel. Finally, a study by Sacks et al. (1995) demonstrated the benefit of seeding microcomposite particles for phase development. An addition of approximately 2 wt% of seed particles could control the formation of fine grained mullite (≤ 0.4 μm) at low temperatures where densification occurs (1300-1400°C) [98]. With the current process of synthesis and comminution, seeding could aid in phase development and densification despite the large endothermic difference caused by separation of the M32 particle reactants.

6. CONCLUSION

This thesis work was to design ceramic paste systems for room temperature deposition via Ceramic On-Demand Extrusion for fabricating dense complex ceramic parts. Overall, this thesis work provided a solid foundation for further development of ceramic paste extrudates compatible with the CODE process.

An oxide-nitride-carbide system for *in situ* fabrication of ZrB_2, as well as an aqueous paste for deposition of single-phase ZrB_2, with two aqueous binders as options for developing an extrudate were presented. Having confirmed a chemistry for reaction sintering, future development is necessary to achieve densification during sintering. Alternative additives, such as boron salts and high char yielding resins, could be used to reach the goal of achieving a high degree of microstructural control.

The development of a high solids loading (50 vol%) yttria-stabilized zirconia paste capable of producing near theoretical density (> 98%) sintered parts was studied. This system is binderless, but also compatible with aqueous binders, and needs further development for suspension stability, increased shelf life and higher solids loading. For dispersion of the 3YSZ an anionic polyelectrolyte was used in an alkaline regime to take advantage of depletion stabilization, but with zeta potential measurements, it is likely a more stable paste could be developed using the same electrolyte in an acidic regime.

A mullite system was developed for the design of a functionally graded composite of mullite and alumina. Due to the sintering temperatures exceeding 1600^oC and multi-hour isothermal holds necessary for primary mullite formation, diphasic mullite powder was synthesized. This premullite composite powder fully transforms into mullite at a temperature of 1440^oC, but becomes significantly more energy intensive if the composite particle is fractured, i.e. milled. Samples that were milled and sintered at 1550^oC for 1 hr exhibited lack-luster relative densities averaging 70.4% of theoretical density. The compacts made from as-synthesized powder, M32, may potentially achieve higher densities through a two-step viscous transient sintering cycle, with isothermal holds at 1300^oC and 1550^oC. Literature also suggests that seeding could aid in phase development at lower sintering temperatures, if the M32 is comminuted for a finer particle size.

7. FUTURE WORK

To add value to this thesis work, quantitative rheological characterization of the paste systems is necessary. Rheological analysis of structured fluids can be done to design a functional paste for a specific application. To begin, it would be necessary to gauge the shelf life and sensitivity of a test batch to the rheological procedure using a solvent trap. This would involve measuring the change in viscosity with a constant shear rate for a fixed time frame, e.g. 5 minutes. Any increase in viscosity is likely due to rapid sedimentation and separation of the paste in a controlled humidity environment. The first test is to determine the high and low resolution of the flow behavior. It includes measuring the flow curve across a broad range of shear rates, e.g. $1.0\text{-}100 \text{ s}^{-1}$, and determining the shear rate with the lowest repeatable viscosity in a sample. This identifies a shear range where the viscosity is most sensitive. Next it would be valuable to determine if a transient viscosity peak is detectable, which can be done by measuring the viscosity curve with different measuring point durations at a low shear rate. One curve should have a set dwell time, e.g. 10 s, and one with logarithmic dwell times, e.g. 50s – 2s, for changing shear rates. A common rule is that for shear rates $\gamma < 1 \text{ s}^{-1}$ the duration (t) at a measured value corresponds to the reciprocal of the set shear-rate, so $t > 1/\gamma$.

Additionally, strain or stress sweeps can be used to determine the change between solid and fluid mechanics, identifying the linear viscoelastic region. This is done by changing the stress or strain amplitude with respect to time. The aim is to describe the deformation behavior of a sample in a non-destructive manner by identifying the upper limit of deformation before flow or shear. The storage behavior and dispersion stability can then be identified by a frequency sweep to describe the time-dependent behavior of the sample. Using the upper limits from the amplitude and frequency sweeps, one can begin to measure the storage modulus (G') and loss modulus (G"), which describe the elastic and viscous portion of the sample fluid mechanics respectively. If G' > G", the sample can be called a viscoelastic solid, having significant potential energy due to chemical or physical interaction in the structure. If G" > G', the sample is a viscoelastic liquid, with energy being dissipated through the interaction of the individual units of the

structure, which are not strongly bonded or linked. Finally, constant dynamic-mechanical conditions can be applied, from the frequency and amplitude tests, to determine any time-dependent behavior of the sample. A similar test, though somewhat extraneous for CODE, could be temperature-dependent behavior. Also a dynamic-mechanical test this test would identify material softening or melting behavior on heating, and solidification, crystallization, or gelation upon cooling.

The characterization results from these tests would provide flow curves showing the change in viscosity with respect to shear rate, the determination of a zero-shear viscosity regime, the paste yield point, the complex moduli, G^*, and sensitivity to shear history. Not only are these parameters necessary for designing complex fluids for advanced deposition applications, but commonly reported in the current literature for concentrated suspensions. Useful publications in literature for designing dynamic rheological tests include Lewis [45], Pugh and Bergstrom [99], and Mezger [100].

Further value could be added to the quantitative understanding of developed pastes by using dynamic light scattering (DLS) techniques to measure the initial average particle size (d_{50}), and to understand the developed network and fracture of the network if applied to dynamic rheological evaluations described above. Small angle light scattering (SALS), which is a lower resolution version of small angle x-ray scattering (SAXS) can provide rheological and structural information, i.e. particle shape, size, orientation, and distribution. This information can be used to tune dispersion strategy and deposition parameters.

APPENDIX
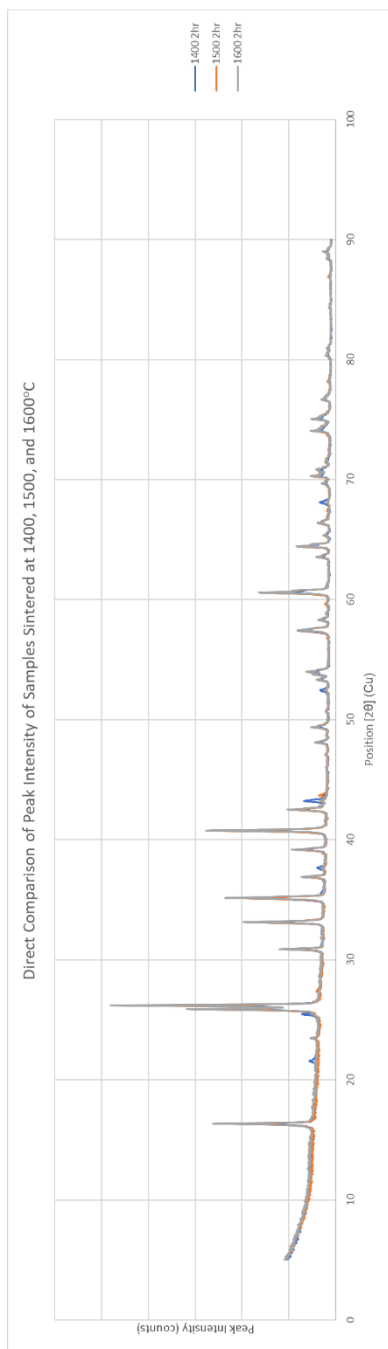
(A)
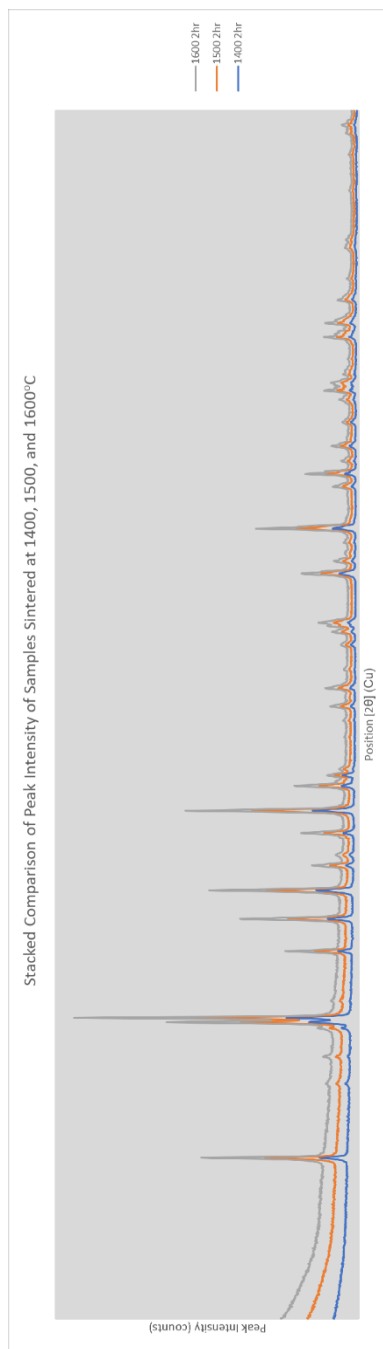
(B)

Figure 1. XRD micrographs showing the evolution of mullite from reaction sintering kaolin: alumina specimens, with mullite formation at 1600°C, compared to 1400°C 2 hr and 1500°C 2 hr in (A). A trend to sharper peaks, indicating full reaction and mullite formation is evident in (B) by viewing a stacked comparison of the data in (A).

REFERENCES

[1] A. Ghazanfari, W. Li, M.C. Leu, G.E. Hilmas, A novel extrusion-based additive manufacturing process for ceramic parts, in: D. Bourell, J. Beaman, R. Crawford, S. Fish, H. Marcus, C. Seepersad (Eds.), Solid Free. Fabr. Symp., Austin, TX, USA, 2016.

[2] J.A. Lewis, "Direct-write assembly of ceramics from colloidal inks," *Current Opinion in Solid State and Materials Science*, 6 (2002) 245-250.

[3] J.A. Lewis, "Direct ink writing of 3D functional materials," Adv. Funct. Mater., 16 [17] 2193-2204 (2006).

[4] P. Miranda, E. Saiz, K. Gryn, and A.P. Tomsia, "Sintering and robocasting of β-tricalcium phosphate scaffolds for orthopaedic applications," Acta Biomaterialia, 2 [4] 457-466 (2006).

[5] A. Zocca, P. Colombo, C.M. Gomes, and J. Gunster, "Additive manufacturing of ceramics: issues, potentialities, and opportunities," J. Am. Ceram. Soc., 98 [7] 1983-2001 (2015).

[6] W.G. Fahrenholtz and G.E. Hilmas, "Refractory diborides of zirconium and hafnium," J. Am. Ceram. Soc., 90 [5] 13-47-1364 (2007).

[7] S.C. Zhang, G.E. Hilmas, and W.G. Fahrenholtz, "Pressureless densification of zirconium diboride with boron carbide additions," J. Am. Ceram. Soc., 89 [5] 1544-50 (2006).

[8] W.G. Fahrenholtz, G.E. Hilmas, S.C. Zhang, and S. Zhu, "Pressureless sintering of zirconium diboride: particle size and additive effects," J. Am. Ceram. Soc., 91 [5] 1398-1404 (2008).

[9] M.N. Rahaman, Ceramic Processing and Sintering, Boca Raton, FL, CRC Press (2003).

[10] X. Zhang, J. Han, and Z. Wang, ZrB2 and ZrB2-based Ceramics, Lexington, KY, LAP Lambert Academic Publishing (2014).

[11] C. Yan, R. Liu, C. Zhang, Y. Cao, and X. Long, "Synthesis of ZrB2 Powders from ZrO2, BN, and C," J. Am. Ceram. Soc., 99 [1] 16-19 (2016).

[12] L. Zoli, A.L. Costa, and D. Sciti, "Synthesis of nanosized zirconium diboride powder via oxide-borohydride solid-state reaction," Scripta Materialia, 109 (2015) 100-103.

[13] S. Leo, C. Tallon, and G.V. Franks, "Aqueous and nonaqueous colloidal processing of difficult-to-densify ceramics: suspension rheology and particle packing," J. Am. Ceram. Soc., 97 [12] 3807-17 (2014).

[14] ASTM F2792-12a, Standard Terminology for Additive Manufacturing Technologies, (Withdrawn 2015), ASTM International, West Conshohocken, PA, 2012, www.astm.org.

[15]   N. Guo and M.C. Leu, "Additive manufacturing: technology, applications and research needs," Front. Mech. Eng., 8 [3] 215-243 (2013).

[16]   M. Vaezi et al., "Multiple material additive manufacturing – part 1: a review," Virtual and Physical Prototyping, 8 [1] 19-50 (2013).

[17]   M. Vaezi, H. Seitz, and S. Yang, "A review on 3D micro-additive manufacturing technologies," Int. J. Adv. Manuf. Technol., 67 (2013) 1721-1754.

[18]   G. Mitteramskogler, R. Gmeiner, R. Felzmann et al., "Light curing strategies for lithography-based additive manufacturing of customized ceramics," Additive Manufacturing, 1-4 [1] 110-118 (2014).

[19]   Y. Liu, W. Hu, F. Qin et al., "Additive manufacturing of three dimensional nanocomposite based objects through multiphoton fabrication," Polymers, 8 [9] 325-339 (2016).

[20]   P. Juskova et al., "Resolution improvement of 3D stero-lithography through the direct laser trajectory programming: application to microfluidic deterministic lateral displacement device," Analytica Chimica Acta, 1000 (2018) 239-247.

[21]   Travitzky et al., "Additive manufacturing of ceramic-based materials," Adv. Eng. Matl., 16 [6] 729-754 (2014).

[22]   S. Rodrigues, R. Chartoff, D. Klostermann et al., "Solid freeform fabrication of functional silicon nitride ceramics by laminated object manufacturing," Solid Freeform Fabrication Symposium Proceedings, 2000.

[23]   Z.C. Eckel, C. Zhou et al., "Additive manufacturing of polymer-derived ceramics," Science, 351 [6268] 58-62 (2016).

[24]   Y. de Hazan and D. Penner, "SiC and SiOC ceramic articles produced by stereolithography of acrylate modified polycarbosilane systems," J. Eur. Ceram. Soc., 37 (2017) 5205-12.

[25]   J. Cesarano III, "A review of robocasting technology," MRS Proceedings, 542 (1998) 133-139.

[26]   B. Tuttle, J. Smay, J. Cesarano III, J.A. Lewis et al., "Robocast Pb(Zr0.95Ti0.05)O3 ceramic monoliths and composites," J. Am. Ceram. Soc., 84 [4] 872-74 (2001).

[27]   J.E. Smay, J. Cesarano III, and J.A. Lewis, "Colloidal inks for directed assembly of 3-D periodic structures," Langmuir, 18 [14] 5429-37 (2002).

[28]   L. Rueschhoff et al., "Additive manufacturing of dense ceramic parts via direct ink writing of aqueous alumina suspensions," Inst. J. Appl. Ceram. Technol., 13 [5] 821-830 (2016).

[29]   M.S. Mason, T. Huang, R.G. Landers, M.C. Leu, and G.E. Hilmas, "Freeform extrusion of high solids loading ceramic slurries, part 1: extrusion process modeling," 17th Annual Solid Freeform Fabrication Symposium, Austin, TX, (2006) 316-328.

[30] M.S. Mason, T. Huang, R.G. Landers, M.C. Leu, and G.E. Hilmas, "Freeform extrusion of high solids loading ceramic slurries, part 2: extrusion process control," 17th Annual Solid Freeform Fabrication Symposium, Austin, TX, (2006) 329-338.

[31] X. Zhao, M.S. Mason, T. Huang et al., "Experimental investigation of effect of environment temperature on freeze-form extrusion fabrication," 18th Annual Solid Freeform Fabrication Symposium, Austin, TX, (2007) 135-146.

[32] T. Huang, M.S. Mason, G.E. Hilmas, and M.C. Leu, "Freeze-form extrusion fabrication of ceramics parts," Virtual and Physical Prototyping, 1 [2] 93-100 (2006).

[33] T. Huang, M.S. Mason, X. Zhao, G.E. Hilmas, and M.C. Leu, "Aqueous-based freeze-form extrusion fabrication of alumina components," Rapid Prototyping, 15 [2] 88-95 (2009).

[34] N.D. Doiphode, T. Huang, M.C. Leu, M.N. Rahaman, and D.E. Day, "Freeze extrusion fabrication of 13-93 bioactive glass scaffolds for bone repair," J. Mater. Sci: Mater. Med., 22 (2011) 515-523.

[35] T. Huang, M.N. Rahaman, N.D. Diophode et al., "Porous and strong bioactive glass (13-93) scaffolds fabricated by freeze extrusion technique," Matl. Sci. and Eng. C, 31 (2011) 1482-49.

[36] M.C. Leu, B.K. Deuser, L. Tang, R.G. Landers, G.E. Hilmas, and J.L. Watts, "Freeze-form extrusion fabrication of functionally graded materials," CIRP Annals, 61 [1] 223-226 (2012).

[37] W. Li et al., "Characterization of zirconia specimens fabricated by Ceramic On-Demand Extrusion," Ceramics International, (2018) https://doi.org/10.1016/j.ceramint.2018.04.008 (in press).

[38] D. Owens et al., "3D printing of ceramic components using a customized 3D ceramic printer," Prog. Addit. Manuf., 1-7 (2018).

[39] C. Murphy, K. Kolan et al., "3D bioprinting of stem cells and polymer/bioactive glass composite scaffolds for bone tissue engineering," Intl. J. Bioprinting, 3 [1] 1-11 (2017).

[40] C. Li, L. Gao, F. Chen, and C. Liu, "Fabrication of mesoporous calcium silicate/calcium phosphate cement scaffolds with high mechanical strength by freeform fabrication system with micro-droplet jetting," J. Mater. Sci., 50 (2015) 7182-91.

[41] R. Moreno, "Colloidal processing of ceramics and composites," Advances in Applied Ceramics, 111 [5-6] 246-253 (2012).

[42] J.S. Reed, Principles of Ceramic Processing, New York, NY, John Wiley & Sons, Inc. (1995).

[43]   S. Briggs and T.W. Healy, "Electrosteric stabilization of colloidal zirconia with low molecular weight polyacrylic acid," J. Chem. Soc. Faraday Trans., 90 [22] 3415-21 (1994).

[44]   D.J. Rojas, P.M. Cleasson et al., "The effect of salt concentration on adsorption of low-charge-density polyelectrolytes and interactions between polyelectrolyte-coated surfaces," J. Colloid Interface Sci., 205 (1998) 77-78.

[45]   J.A. Lewis, "Colloidal processing of ceramics," J. Am. Ceram. Soc., 83 [10] 2341-59 (2000).

[46]   H.M. Wyss, E.V. Tervoort, and L.J. Gauckler, "Mechanics and microstructures of concentrated particle gels," J. Am. Ceram. Soc., 88 [9] 2337-48 (2005).

[47]   A.R. Studart, E. Amstad, and L.J. Gauckler, "Colloidal stabilization of nanoparticles in concentrated suspensions," Langmuir, 23 (2007) 1081-90.

[48]   R.L. Coble, "Sintering crystalline solids I. intermediate and final state diffusion models," J. App. Physics, 32 [5] 787-792 (1961).

[49]   R.L. Coble, "Sintering crystalline solids II. Experimental test of diffusion models in powder compacts," J. App. Physics, 32 [5] 793-799 (1961).

[50]   I.W. Chen and X.H. Wang, "Sintering dense nanocrystalline ceramics without final-stage grain growth," Nature, 404 (2000) 168-171.

[51]   R.M. German, *Liquid Phase Sintering*, Troy, NY, Springer (1985).

[52]   L.C. De Jonghe and M.N. Rahaman, Sintering of Ceramics, in Handbook of Advanced Ceramics, Vol.1: Materials Science, S. Somiya, F. Aldinger, N. Claussen, R.M. Spriggs, K. Uehino, K. Koumoto, M. Kaneno, Elsevier, New York, (2003) chap. 4.

[53]   C.R. Bickmore and R.M. Laine, "Synthesis of oxynitride powders via fluidized-bed ammonolysis, part I: large, porous, silica particles," J. Am. Ceram. Soc. 79 [11] 2865-77 (1996).

[54]   P. Grammatikopoulos et al., "Nanoparticle design by gas-phase synthesis," Adv. In Physics, 1 [1] 81-100 (2016).

[55]   P.D.D. Rodrigo and P. Boch, "High purity mullite ceramics by reaction sintering," Int. J. High Technology Ceramics, 1 (1985) 3-30.

[56]   T. Lapauw et al., "Synthesis of the new MAX phase Zr2AlC," J. Eur. Ceram. Soc., 36 [8] 1847-53 (2016).

[57]   W.G. Fahrenholtz, "Reactive processing in ceramic-based systems," Int. J. Appl. Ceram. Technol., 3 [1] 1-12 (2006).

[58]   N.L. Okamoto, M. Kusakari, K. Tanaka, H. Inui, and S. Otani, "Anisotropic elastic constants and thermal expansivities in monocrystal CrB2, TiB2, and ZrB2," Acta Materialia, 58 (2010) 76-84.

[59]   A.L. Chamberlain, W.G. Fahrenholtz, and G.E. Hilmas, "Pressureless sintering of zirconium diboride," J. Am. Ceram. Soc., 89 [2] 450-456 (2006).

[60]   A. Li, A.S. Thornton, B. Deuser, J. Watts, M.C. Leu, G.E. Hilmas, and R.G. Landers, "Freeze-form extrusion fabrication of functionally graded material composites using zirconium carbide and tungsten," Solid Free. Fabr. Symp., Austin, TX, USA (2012).

[61]   S. Zhu, W. G. Fahrenholtz, G. E. Hilmas, and S.C. Zhang, "Pressureless sintering of zirconium diboride using boron carbide and carbon additions," J. Am. Ceram. Soc., 90 [11], 3660–63 (2007).

[62]   I.A. Aksay, D.M. Dabbs, and M. Sarikaya, "Mullite for structural, electronic, and optical applications," J. Am. Ceram. Soc., 74 [10] 2343-58 (1991).

[63]   J .Roy, S. Das, and S. Maitra, "Solgel-processed mullite coating- a review," Int. J. Appl. Ceram. Technol., 12 [S2] E71-E77 (2015).

[64]   W.C. Wei and J.W. Halloran, "Phase transformation of diphasic aluminosilicate gels," J. Am. Ceram. Soc., 71 [3] 166-72 (1988).

[65]   K. Okada, "Activation energy of mullitization from various starting materials," J. Eur. Ceram. Soc., 28 [2] 377-82 (2008).

[66]   A.M. Buckley and M. Greenblatt, "The sol-gel preparation of silica gels," J. Chem. Ed., 71 [7] 599-602 (1994).

[67]   L. Pavlovic, S. Matinovic, A. Terzic, "Influence of mineralizers on mullite synthesis," Am. Ceram. Soc. Bull., 85 [11] 9301-9306 (2006).

[68]   L.B. Kong, Y.Z. Chen, T.S. Zhang, J. Ma, F. Boey, H. Huang, "Effect of alkaline-earth oxides on phase formation and morphology development of mullite ceramics," Cer. Intl., 30 (2004) 1319-1323.

[69]   J. Chevalier et al., "The tetragonal-monoclinic transformation in zirconia: lessons learned and future trends," J. Am. Ceram. Soc., 92 [9] 1901-1920 (2009).

[70]   J.R. Kelly and I. Denry, "Stabilised zirconia as a structural ceramic: an overview," Dental Materials, 24 (2008) 289-298.

[71]   C. Sun and X. Zhang, "The influences of the material properties on ceramic micro-stereolithography," Sensors and Actuators A, 101 (2002) 364-370.

[72]   ASTM, Standard Test Method for Water Absorption, Bulk Density, Apparent Porosity, and Apparent Specific Gravity of Fired Whiteware Products, Ceramic Tiles, and Glass Tiles. No. ASTM C373- 14A (2014).

[73]   T. Huang, Fabrication of ceramic components using freeze-form extrusion fabrication, Ph.D., University of Missouri – Rolla, 68 (2007) 3326.

[74]   T. Huang, G.E. Hilmas, and W.G. Fahrenholtz, "Dispersion of zirconium diboride in an aqueous, high-solids paste," Int. J. Appl. Ceram. Technol., 4 [5] 470-479 (2007).

[75] V.L. Wiesner, L.M. Rueschhoff et al., "Producing dense zirconium diboride components by room-temperature injection molding of aqueous ceramic suspensions," Ceramics International, 42 (2016) 2750-60.

[76] ASTM, Standard Test Method for Flexural Strength of Advanced Ceramics at Ambient Temperature. No. ASTM C1161-18 (2018).

[77] E. Feilden et al., 3D printing bioinspired ceramic composites," Scientific Reports, 7 (2017) article number: 13759.

[78] W.M. Guo and G.J. Zhang, "Reaction processes and characterization of ZrB2 powder prepared by boro/carbothermal reduction of ZrO2 in vacuum," J. Am. Ceram. Soc., 92 [1] 264-267 (2009).

[79] Y. Miao, Z. Yang et al., "A novel in situ synthesis of SiBCN-Zr composites prepared by a sol-gel process and spark plasma sintering," Dalton Trans., 45 (2016) 123739-12744.

[80] C. Yan, C. Zhang, Y. Cao, and X. Long, "Synthesis of ZrB2 powders from ZrO2, BN, and C," J. Am. Ceram. Soc., 99 [1] 16-19 (2016).

[81] A. Ghazanfari, W. Li, D. McMillen et al., "Additive manufacturing and mechanical characterization of high-density, fully stabilized zirconia," Ceramics International, 43 [8] 6082-88 (2017).

[82] W. Li, A. Ghazanfari, D. McMillen, M. C. Leu, and G. E. Hilmas, "Fabricating ceramic components with water dissolvable support structures by the Ceramic On-Demand Extrusion process," CIRP Annals, 66 [1] 225-228 (2017).

[83] W. Li et al., "Fabricating parts with organic support material by the ceramic on-demand extrusion process," in Proceedings of the 28th Annual International Solid Freeform Fabrication Symposium, (2017) 605-615.

[84] W. Hertl, "Surface chemistry of zirconia polymorphs," Langmuir, 5 (1989) 96-100.

[85] T. Cao, I. Szilagyi et al., "Aggregation of colloidal particles in the presence of the multivalent co-ions: the inverse Schulze-Hardy rule," Langmuir, 31 (2015) 6610-14.

[86] Y. Rao, "Nanofluids: stability, phase diagram, rheology, and applications," Particuology, 8 (2000) 549-555.

[87] J.C. Conrad, S.R. Ferreira et al., "Designing colloidal suspensions for directed materials assembly," Current Opinion in Colloid & Interface Science, 6 (2010) 71-79.

[88] Y.F. Chen, M.C. Wang, and M.H. Hon, "Transformation kinetics for mullite in kaolin-Al2O3 ceramics," J. Mater. Res., 18 [6] 1355-1362 (2003).

[89] C.Y. Chen, G.S. Lan, and W.H. Tuan, "Preparation of mullite by reaction sintering of kaolinite and alumina," J. Eur. Ceram. Soc., 20 (2000) 2519-2525.

[90]   C.Y. Chen and W.H. Tuan, "The processing of kaolin powder compact," Ceramics International, 27 (2001) 795-800.

[91]   G.Orange, G. Fantozzi et al., "High temperature mechanical properties of reaction-sintered mullite/zirconia and mullite/alumina/zirconia composites," J. Mat. Sci., 20 (1985) 2533-40.

[92]   L.S. Cividanes, T.M.B. Campos et al., "Review of mullite synthesis routes by sol-gel method," J. Sol-Gel Sci. Technol., 55 (2010) 111-125.

[93]   J.C. Huling and G.L. Messing, "Hybrid gels for homoepitactic nucleation of mullite," J. Am. Ceram. Soc., 72 [9] 1725-29 (1989).

[94]   H. Schneider, *Mullite*, Weinheim, BW, Germany, WILEY-VCH (2003).

[95]   K. Wang and M.D. Sacks, "Mullite formation by endothermic reaction of α-alumina/silica microcomposite particles," J. Am. Ceram. Soc., 79 [1] 12-16 (1996).

[96]   W.C. Wei and J.W. Halloran, "Transformation kinetics of diphasic aluminosilicate gels," J. Am. Ceram. Soc., 71 [7] 581-87 (1988).

[97]   M.D. Sacks, G.W. Scheiffeler et al., "Fabrication of ceramics and composites by various transient viscous sintering of composite particles," Ceramics Transactions, "22 (1991) 437-455.

[98]   M.D. Sacks, Y.J. Lin, G.W. Scheiffele, K. Wang, and N. Bozkurt, "Effect of seeding on phase development, densification behavior, and microstructure evolution in mullite fabricated from microcomposite particles," J. Am. Ceram. Soc., 78 [11] 2897-906 (1995).

[99]   R.J. Pugh and L. Bergstrom, "Rheology of concentrated suspensions." Surface and Colloid Chemistry in Advanced Ceramics Processing. 1 [51] L. Bergstrom. New York: MARCEL DEKKER, (1994) 192-244.

[100]   T.G. Mezger, *Applied Rheology*. Graz, Austria, Anton Paar (2014).

VITA

Devin McMillen attended high school at East Newton R-VI and graduated in the spring of 2009. He moved to Joplin, Missouri to attend Missouri Southern State University, partaking in the Honors Program as a chemistry major. After completing one year, Devin transferred to the Missouri University of Science and Technology to pursue a degree in ceramic engineering. While an undergraduate student Devin participated in department recruitment opportunities, giving demos to prospective students; he also worked as a PRO Leader for four years in the office of Enrollment Management's Student Success Programs; as well as, a co-op with Biomet, Inc. and an internship with DalTile Corp.. Devin received his B.S. degree in Ceramic Engineering from the Missouri University of Science and Technology in May 2015.

Devin began his graduate work as a Master's student for Dr. Ming C. Leu at Missouri University of Science and Technology in May 2015. During his graduate career, Devin focused on materials development for the extrusion-based additive manufacturing technique, Ceramic On-Demand Extrusion. His research has been featured and presented at the 27th and 28th Annual International Solid Freeform Fabrication Symposium in Austin, TX. While a graduate student, his research team published over five publications relating to the additive manufacturing of functional, technical ceramics. He also mentored two undergraduate NSF-REU students in the summer semesters of 2016 and 2017. Devin received his M.S. degree in Manufacturing Engineering from Missouri University of Science and Technology in July 2018.